A thermo-hydromechanical damage model and its application to a deep geological radioactive repository

Zhan Yu, Jian-Fu Shao, Minh-Ngoc Vu

A thermo-hydromechanical damage model and its application to a deep geological radioactive repository

Zhan YU[a], Jian-Fu SHAO[a,b,*], Minh-ngoc VU[c]

[a] *University of Lille, CNRS, EC Lille, LaMcube, UMR9013, 59000 Lille, France*
[b] *Institut Universitaire de France (IUF), France*
[c] *Andra, Chatenay Malabry, France*

Abstract

This study conducts a numerical analysis of long-term thermo-hydromechanical (THM) processes, with a particular focus on deep geological disposal of radioactive waste. It emphasizes the modeling of damage zones resulting from excavation activities, as well as changes in pore pressure and temperature. The numerical model presented in this paper delineates the fundamental relations of thermo-poro-elasticity. It also introduces a double phase field method specifically formulated for rock materials, taking into account THM coupling and time-dependent behavior. The proposed method has been implemented in a finite element code and applied to a benchmark problem associated with the French High-Level Waste (HLW) disposal concept. This application centers on the numerical analysis of THM responses and the progression of induced cracks, utilizing the proposed model. The occurrence of damage in the far field can be more readily attributed to the boundary conditions on the distant side, which are affected by the spacing between every two repositories. Additionally, time-dependent behavior significantly impacts the long-term scenario.

Keywords: Radioactive waste, geological disposal, thermo-hydromechanical coupling, Callovo-Oxfordian claystone, damage and cracking, phase-field method

*Corresponding author: jian-fu.shao@polytech-lille.fr

1. Introduction

Geological disposal is a strategy considered by many countries for the management of radioactive waste. In this regard, understanding the short-term and long-term thermo-hydromechanical (THM) responses of the geological barrier becomes essential. In France, the French national agency for radioactive waste management (Andra) has established an underground research laboratory (URL) in Bure. This URL, located within the Callovo-Oxfordian (COx) claystone layer at an average depth of 490 meters, plays a pivotal role in investigating the THM responses of the host rock, as outlined in the work by [1].

To thoroughly investigate the characteristics of the thermo-hydromechanical responses of the host rock during various phases of geological disposal, as well as to evaluate the feasibility of constructing and operating a disposal site within the COx claystone formation, a two-pronged approach has been employed. On one hand, extensive experimental studies at the sample scale have been conducted to examine the primary properties of COx claystone. These investigations cover a wide range of aspects including its basic deformation and failure behavior [2, 3, 4], time-dependent deformation [5, 6, 7], thermo-hydraulic effects [8, 9, 10], thermal cracking under saturated conditions [6, 11, 12, 13, 14], among others. On the other hand, a series of in-situ experiments have been carried out at the Andra URL [1, 15, 14, 16]. A variety of heating experiments, ranging from small-scale to full-scale, have been carried out at the URL. These significant studies have led to a consensus on several key issues. Notably, due to the thermal expansion coefficient disparity between pore water (ranging from 2.3×10^{-4} K^{-1} at 20°C to 7.2×10^{-4} K^{-1} at 90°C) and the solid skeleton of the COx claystone (1.5×10^{-5} K^{-1}) [6, 11, 12], the pore water pressure in the surrounding saturated claystone increases with the temperature rise caused by the heat emission from High-Level Waste (HLW) packages. This induced overpressure in the pore water leads to a slow water flow phase due to the low permeability of the host rock, estimated between 1.0×10^{-21} m^2 and 2.0×10^{-20} m^2 [17, 18]. Given that these phenomena could potentially jeopardize the stability of the host rock, it is crucial to meticulously study and verify the crack process induced by the complex thermo-hydromechanical coupling behavior in both the short and long term of geological disposal.

To specifically tackle the THM coupling challenges associated with the geological disposal of radioactive waste, the international research project DECOVALEX was established and has been operational for several decades. Significant advancements have been made through this initiative, with a comprehensive overview available in references [19, 20, 21]. Notably, a variety of approaches, both continuous and discontinuous, have been proposed to address THM coupling problems in both saturated and partially saturated porous media, employing both elastic and inelastic models, as detailed in [22, 23, 24]. In this study, the primary focus is on analyzing the cracking and damage processes in both of near and far field of the repository, specifically under coupled thermo-hydromechanical conditions. Over the past decades, a range of numerical methods has been developed to model crack initiation and propagation. Notable among these are the Extended Finite Element Method (XFEM), which utilizes a global enrichment technique to represent discontinuities caused by cracks or fractures [25, 26, 27], and the Enriched Finite Element Method (EFEM), employing a local enrichment

solution with elementary sharp functions [28, 29, 30, 31]. The theory of peridynamics (PD) is a non-local continuum theory based on integro-differential equations [32, 33, 34]. In more recent developments, drawing on the variational principle of fracture mechanics as outlined by [35], a novel numerical solution known as the phase-field method has been introduced [36, 37]. The phase-field method, with its ability to approximate sharp fractures via a regularized, smeared crack density field, is particularly adept at managing the nucleation and propagation of cracks. It emerges as an effective approach for capturing the transition from diffuse damage to localized cracks. Owing to its compact and coherent framework, this method shows significant potential for addressing more complex cracking challenges, such as those induced by THM coupling. In domain of rock mechanics, various specific models have been developed for addressing cracking in brittle-ductile behavior [38, 39, 40]. The phase-field method has also been applied to cracking modeling with thermo-hydromechanical coupling [41, 42, 43].

In this paper, we shall present a short summary of numerical modeling framework of thermo-hydromechanical responses considering time dependent behavior and induced cracking processes in the context of deep geological disposal of radioactive waste. As a part work of DECOVALEX-2023 (Task A), the benchmark of parallel, sub-horizontal micro-tunnels (called HLW disposal cells) drilled from access drifts in the COx formation is considered to simulate and analysis. The main objective is to improve the ability of numerical models to predict processes and mechanisms of fracture initiation and growth in claystones due to a rapid increase of heat overpressure. In this study, the viscoplastic model and the damage model, utilizing the phase-field method, are integrated to address THM coupled problems in saturated porous media, taking into account both damage effects and time-dependent behavior. This combined model has been successfully applied to simulate an in-situ heating test, allowing for the distinct identification of damage zones induced by excavation, heating, and creep behavior. The simulation outcomes provide valuable insights for analyzing and evaluating the design of underground HLW packages.

2. Fundamental relations of thermo-poro-elasticity

In this section, we outline the key relations that form the basis of thermo-poro-elastic coupling analysis. For simplicity and clarity, our discussion is confined to scenarios involving saturated materials. The saturated porous medium occupies a volume denoted as Ω and is bounded by an external boundary$\partial\Omega$. The thermo-hydromechanical behavior of this material is described through three distinct physical fields:
(i) Within the mechanical field, there exists a body force $\mathbf{f}_b$ throughout Ω, a surface force $\mathbf{t}_N$ acting on part of the external boundary $\partial\Omega_f$, and a prescribed displacement $\overline{\mathbf{u}}$ on the complementary part of the external boundary $\partial\Omega_u$.
(ii) For the pore fluid pressure field, the fluid flux $\overline{\omega}$ is present on the external boundary $\partial\Omega_\omega$, alongside a prescribed fluid pressure $\overline{p}$ on the external boundary $\partial\Omega_p$.
(iii) In the temperature field, the heat flux $\overline{\mathbf{q}}$ occurs on the external boundary $\partial\Omega_q$, with a prescribed temperature change $\overline{\theta}$ on the external boundary $\partial\Omega_\theta$.
Therefore, the constitutive relations pertinent to thermo-poro-elastic theory, as outlined in

key references such as [44, 45], can be expressed as follows:

$$\begin{cases} \boldsymbol{\sigma} - \boldsymbol{\sigma}_0 = \mathbb{C}_b : \boldsymbol{\varepsilon}^e - \boldsymbol{B}(p - p_0) - \boldsymbol{A}_b\theta \\ p - p_0 = M(-\boldsymbol{B} : \boldsymbol{\varepsilon}^e + \frac{m}{\rho_f^0}) + 3\alpha_m M\theta \\ s - s_0 = s_m^0 m + \boldsymbol{\alpha}_b : (\boldsymbol{\sigma} - \boldsymbol{\sigma}^0) - (3\alpha_m - \boldsymbol{B} : \boldsymbol{\alpha}_b)(p - p_0) + \frac{C_\sigma^b}{T_0}\theta \end{cases} \tag{1}$$

with stress tensor $\boldsymbol{\sigma}^0$, fluid pressure p_0, entropy s_0, temperature T_0 and volumetric density of fluid ρ_f^0 at the initial reference configuration. In the order of appearance, $\mathbb{C}_b$ is the forth order elastic stiffness tensor in drained condition. $\boldsymbol{B}$ is the second order tensor of Biot coefficients, while the scalar coefficient M is the Biot modulus. $\boldsymbol{\alpha}_b$ and $\boldsymbol{A}_b$ are two second order tensors respectively for thermal dilatation and thermo-elastic coupling coefficients in drained condition. θ is the variation of temperature, which has $\theta = T - T_0$. The coefficient α_m denotes the differential thermal dilation of saturated porous medium. C_σ^b is the volumetric specific heat for constant stress under drained condition. In the case of isotropic materials, one has $\mathbb{C}_b^0 = 3K_b\mathbb{J} + 3\mu_b\mathbb{K}$, with K_b^0 and μ_b^0 being the drained bulk and shear modulus respectively. The other coefficients are also simplified as follows: $\boldsymbol{B} = b\boldsymbol{\delta}$, $\boldsymbol{\alpha_b} = \alpha_b\boldsymbol{\delta}$ and $\boldsymbol{A}_b = 3K_b\alpha_b\boldsymbol{\delta}$. The Biot modulus is given by $1/M = (b - \phi)/K_m + \phi/K_f$, with K_m being the bulk modulus of solid matrix, K_f that of fluid and ϕ porosity. The differential thermal dilation coefficient is expressed $\alpha_m = (b - \phi)\alpha_b + \phi\alpha_f$ with the thermal dilation coefficient of the fluid α_f.

Utilizing the momentum balance equation, Darcy's fluid conduction law, fluid mass conservation, Fourier's heat conduction law, and the energy balance relation, the following governing equations for boundary value problems are derived:

$$\begin{cases} div\boldsymbol{\sigma} + \mathbf{f}_b = 0 \\ div(\dfrac{\boldsymbol{\kappa}}{\mu_f} : \nabla p) = \dfrac{1}{M}\dfrac{\partial p}{\partial t} + \dfrac{\partial(\boldsymbol{B} : \boldsymbol{\epsilon})}{\partial t} - 3\alpha_m\dfrac{\partial\theta}{\partial t} \\ div(\boldsymbol{\lambda} : \nabla\theta) = \dfrac{1}{C_\epsilon^b}\dfrac{\partial\theta}{\partial t} - 3\alpha_m T_0\dfrac{\partial p}{\partial t} + T_0\dfrac{\partial(\boldsymbol{A}_b : \boldsymbol{\epsilon})}{\partial t} \end{cases} \tag{2}$$

where $\boldsymbol{\kappa}$ and $\boldsymbol{\lambda}$ are respectively the permeability and heat conductivity tensors. The symbol μ_f represents the dynamic viscosity of the fluid, while C_ϵ^b denotes the specific heat of the porous medium under constant volume and drained conditions. It should be noted that in the third relation, the heat convection term associated with fluid flow is omitted. Once specific boundary and initial conditions are established, these governing equations can then be solved for the given boundary value problems.

3. Phase-field method for saturated porous media

In the context of geological disposal of radioactive waste, excavation activities, temperature fluctuations, and increases in water and gas pressure can lead to the formation of damaged and cracked zones. Consequently, accurately describing the initiation and evolution of these zones over both short and long terms becomes essential. This section presents the formulation of a specialized phase-field model, designed specifically for rock materials.

This model incorporates thermo-hydromechanical coupling and accounts for time-dependent behavior.

As this approach has been frequently encountered in the literature, the author opts to maintain a straightforward and concise writing style. This decision is made to facilitate easier reading, focusing primarily on highlighting the critical assumptions made and their subsequent consequences.

3.1. Regularized description of crack evolution

The phase-field method originates from the variational principle of fracture mechanics, as proposed by [35]. Its numerical implementation is achieved by approximating the sharp crack topology with a regularized, smeared crack distribution, a technique further elaborated in works by [36, 37]. This approach conceptualizes the nucleation and propagation of quasi-static cracks as the minimization of an energy function, which includes both the stored energy and the energy required for crack formation. This variational framework is aptly suited for extension to address the crack process in saturated porous materials subjected to THM loads. Accordingly, the total energy functional within this context is formulated as follows:

$$E(\boldsymbol{\varepsilon}^e, \boldsymbol{\varepsilon}^{vp}, m^e, m^{vp}, \theta, \Gamma) = E_e(\boldsymbol{\varepsilon}^e, m^e, \theta, \Gamma) + E_{vp}(\boldsymbol{\varepsilon}^{vp}, m^{vp}, \theta, \Gamma) + E_c(\Gamma) \tag{3}$$

where $E_c(\Gamma)$ denotes the fracture surface energy, while $E_e(\boldsymbol{\varepsilon}^e, m^e, \theta, \Gamma)$ denotes the elastic strain energy of cracked material, which is a function of elastic strain tensor $\boldsymbol{\varepsilon}^e$, elastic and viscoplastic fluid mass change per unit initial volume m^e and m^{vp}, variation of temperature θ, as well as the set of crack Γ. $E_{vp}(\boldsymbol{\varepsilon}^{vp}, m^{vp}, \theta, \Gamma)$ denotes the viscoplastic energy of cracked material, which is due to m^{vp}, θ and viscoplastic strain tensor $\boldsymbol{\varepsilon}^{vp}$. It is important to note that, for the sake of completeness, the energy functional is presented here in its most general form. Within this framework, it is assumed that viscoplastic flow contributes to an irreversible change in fluid mass, denoted as m_{vp}. However, it should be recognized that this is not applicable for a purely deviatoric viscoplastic flow in an isotropic material.

Adopting the regularization approach outlined by [36], the state of cracks is denoted by a scalar-valued auxiliary variable $d(\mathbf{x})$, which assumes a value of one on the crack surface and diminishes to zero in an intact state. Consequently, the total area of sharp crack surfaces within the volume Ω is approximated through the volume integration of a crack surface density γ. Moreover, to effectively address mixed-mode cracks in rock-like materials, a double phase field method, as proposed in [46], is employed. This method introduces two distinct parameters: tensile damage d^t and shear damage d^s. Based on this approach, the approximated crack surface area within the volume Γ can be mathematically represented as follows:

$$A_\Gamma \approx A^t_\Gamma(d^t) + A^s_\Gamma(d^s) = \int_\Omega \{\gamma^t(d^t, \nabla d^t) + \gamma^s(d^s, \nabla d^s)\} d\Omega \tag{4}$$

Here, the total surface area of a sharp crack, denoted as A_Γ, is approximated by the volumetric integration of crack density functions for both tensile cracks $\gamma^t(d^t, \nabla d^t)$ and shear cracks $\gamma^s(d^s, \nabla d^s)$. Among the three commonly used phase-field models proposed by [36, 47, 48],

the formulation by [47], which is thermodynamically consistent, is selected for adoption. This formulation can be expressed as follows:

$$\gamma^{\alpha}(d^{\alpha}, \nabla d^{\alpha}) = \frac{1}{2}\{\frac{1}{l_d}(d^{\alpha})^2 + l_d \nabla d^{\alpha}.\nabla d^{\alpha}\} \quad ; \quad \alpha = t, s \tag{5}$$

where l_d represents a length scale parameter that correlates with the width of the smeared cracks. The crack density functions are denoted by $\gamma^{\alpha}(d^{\alpha}, \nabla d^{\alpha})$ and depend on both the damage variables d^{α} and their gradients ∇d^{α}. This non-local formulation aids in regularizing the issues related to damage localization. Utilizing this approximation, Equation (3) can be reformulated as follows:

$$\begin{aligned} E(\boldsymbol{\varepsilon}^e, \boldsymbol{\varepsilon}^{vp}, m, \theta, d^t, d^s) = &\int_{\Omega} w_e(\boldsymbol{\varepsilon}^e, m^e, \theta, d^t, d^s) d\Omega \\ &+ \int_{\Omega} w_{vp}(\boldsymbol{\varepsilon}^{vp}, m^{vp}, \theta, d^t, d^s) d\Omega \\ &+ \int_{\Omega} w_c(d^t, d^s, \nabla d^t, \nabla d^s) d\Omega \end{aligned} \tag{6}$$

with elastic strain energy of cracked material w_e, and the energy density per unit volume requested to create the crack w_c:

$$w_c(d^t, d^s, \nabla d^t, \nabla d^s) = g_c^t \gamma^t(d^t, \nabla d^t) + g_c^s \gamma^s(d^s, \nabla d^s) \tag{7}$$

3.1.1. Elastic stored energy

To incorporate the impacts of pore fluid pressure and temperature variation on crack evolution, the elastic free energy for an intact porous medium is conveniently articulated as follows, utilizing the constitutive relations outlined in Equation (1):

$$w_e^0(\boldsymbol{\varepsilon}^e, p, \theta) = \frac{1}{2}\boldsymbol{\sigma}_b : \boldsymbol{\varepsilon}^e + \frac{1}{2}\frac{(p - p_0)^2}{M} - \frac{1}{2}\frac{C_{\sigma}^b}{T_0}\theta^2 \tag{8}$$

$\boldsymbol{\sigma}^b$ is the Biot (elastic) effective stress tensor given by:

$$\boldsymbol{\sigma}^b = (\boldsymbol{\sigma} - \boldsymbol{\sigma}^0) + \boldsymbol{B}(p - p_0) \tag{9}$$

In most rock types, the evolution of tensile cracks is typically driven by tensile effective stress. Consequently, the Biot effective stress tensor is separated into a positive (tensile) component and a negative (compressive) component, represented as: $\boldsymbol{\sigma}^b = \boldsymbol{\sigma}^{b+} + \boldsymbol{\sigma}^{b-}$. This decomposition is achieved by employing spectral operators $\mathbb{P}_{\sigma}^{\pm}$ [49]:

$$\begin{cases} \boldsymbol{\sigma}^{b+} = \mathbb{P}_{\sigma}^{+} : \boldsymbol{\sigma}^b \\ \boldsymbol{\sigma}^{b-} = \mathbb{P}_{\sigma}^{-} : \boldsymbol{\sigma}^b \end{cases} \tag{10}$$

Accordingly, the elastic strain energy is rewritten as follows:

$$w_e^0(\boldsymbol{\varepsilon}^e, p, \theta) = w_e^{0+}(\boldsymbol{\varepsilon}^e) + w_e^{0-}(\boldsymbol{\varepsilon}^{\boldsymbol{e}}) + \frac{1}{2}\frac{(p - p^0)^2}{M} - \frac{1}{2}\frac{C_{\sigma}^b}{T_0}\theta^2 \tag{11}$$

with

$$\begin{cases} w_e^{0+} = \frac{1}{2}\boldsymbol{\sigma}^{b+} : \boldsymbol{\varepsilon}^{\boldsymbol{e}} \\ w_e^{0-} = \frac{1}{2}\boldsymbol{\sigma}^{b-} : \boldsymbol{\varepsilon}^{\boldsymbol{e}} \end{cases} \tag{12}$$

The model further assumes that tensile cracks predominantly affect the positive stress-related component of the elastic strain energy, whereas shear cracks impact the negative stress-related component. For simplification purposes, the effects of induced cracks on the Biot modulus M and the specific heat C_σ^b are omitted in this analysis. Consequently, the elastic strain energy for materials with cracks is formulated as follows:

$$w_e(\boldsymbol{\varepsilon}^e, p, \theta, d^t, d^s) = h_t(d^t) w_e^{0+} + h_s(d^s) w_e^{0-} + \frac{1}{2}\frac{(p-p_0)^2}{M} - \frac{1}{2}\frac{C_\sigma^b}{T_0}\theta^2 \tag{13}$$

h_t and h_s are two degradation functions of elastic energy due to crack evolution. The following widely used form is here adopted:

$$h_\alpha(d^\alpha) = (1-k)(1-d^\alpha)^2 + k \quad ; \quad \alpha = t, s \tag{14}$$

The small positive constant k is introduced to avoid numerical fluctuation when the material is fully broken ($d^\alpha = 1$).

3.1.2. Viscoplastic deformation

Viscoplastic theory is employed here to characterize time-dependent deformation. As previously discussed, the elastic strain in saturated porous media is influenced by Biot's effective stress. However, plastic or viscoplastic deformations are typically governed by the stress tensor and fluid pressure independently. The complete validation and applicability of the effective stress concept in these scenarios have not been fully established yet. Nonetheless, to simplify the formulation of plastic and viscoplastic models, several micro-mechanical and experimental studies have focused on determining the plastic yield or strength criteria for saturated rock-like materials, as evidenced in works by [50, 51, 52]. It has been established that Terzaghi's effective stress concept provides an effective approximation for accounting for the impact of fluid pressure. This concept is defined as $\boldsymbol{\sigma}^t = \boldsymbol{\sigma} + p\boldsymbol{I}$, where $\boldsymbol{I}$ represents the second-order unit tensor. Consequently, in this study, it is assumed that viscoplastic flow is driven by Terzaghi's effective stress. Moreover, given the focus on the description of damage fields, a straightforward viscoplastic model based on Lemaitre's law is employed, similar to approaches used in previous studies on clayey rocks [53]. Assuming small strain conditions, the total strain increment $d\boldsymbol{\varepsilon}$ is conceptualized as the sum of its elastic and viscoplastic components:

$$d\boldsymbol{\varepsilon} = d\boldsymbol{\varepsilon}^e + d\boldsymbol{\varepsilon}^{vp} \tag{15}$$

The increment of viscoplastic strain $d\boldsymbol{\varepsilon}^{vp}$ is calculated from its flow rate $\dot{\boldsymbol{\varepsilon}}_{vp}$:

$$d\boldsymbol{\varepsilon}^{vp} = \dot{\boldsymbol{\varepsilon}}^{vp} dt \tag{16}$$

Furthermore, the viscoplastic flow rate tensor is assumed to be co-axial with the deviatoric stress tensor, that is:

$$\dot{\boldsymbol{\varepsilon}}^{vp} = \frac{2}{3}\frac{\dot{\varepsilon}_{vp}}{q}\boldsymbol{s}^t \tag{17}$$

q represents the conventional deviatoric stress and is defined as $q = \sqrt{3\boldsymbol{s}^t : \boldsymbol{s}^t/2}$, where $\boldsymbol{s}^t$ is the deviatoric component of Terzaghi's stress tensor $\boldsymbol{\sigma}^t$. The rate of viscoplastic strain is quantified by the scalar variable $\dot{\varepsilon}_{vp}$. This rate is dependent on the current value of the deviatoric stress q and the extent of accumulated viscoplastic strain, which can be described as follows:

$$\dot{\varepsilon}_{vp} = \eta\langle\frac{q-\sigma_s}{\sigma_{ref}}\rangle_+^n(1-\varepsilon_{vp}^{eq})^m \tag{18}$$

where the parameter η represents the viscosity and controls the initial rate of viscoplastic flow. σ_s signifies the threshold stress required to initiate viscoplastic flow. σ_{ref} is a reference stress, with the unit of stresses adopted here being 1 Pa, to ensure the term under the power law remains dimensionless. The material parameters n and m are responsible for controlling the rate of evolution of the viscoplastic flow. Additionally, the scalar variable ε_{vp}^{eq} denotes the equivalent viscoplastic strain, which is defined as follows:

$$\varepsilon_{vp}^{eq}(t) = \int_0^t \sqrt{\frac{2}{3}\dot{\boldsymbol{\varepsilon}}^{vp}(\tau) : \dot{\boldsymbol{\varepsilon}}^{vp}(\tau)}d\tau \tag{19}$$

The viscoplastic energy dissipation density of an intact material can be calculated by:

$$w_{vp}^0(\boldsymbol{\varepsilon}^{vp}) = \int_0^t \boldsymbol{\sigma}^t(\tau) : \dot{\boldsymbol{\varepsilon}}^{vp}(\tau)d\tau \tag{20}$$

In this straightforward model, only shear viscoplastic strains are generated. Consequently, it is a reasonable assumption that viscoplastic dissipation is predominantly affected by the growth of shear cracks. For the purposes of this study, the viscoplastic-damage coupling function is represented using the following simplified form:

$$w_{vp}(\boldsymbol{\varepsilon}^{vp}, d^s) = \chi h_s(d^s) w_{vp}^0(\boldsymbol{\varepsilon}^{vp}) \tag{21}$$

where the parameter χ defines the effect of shear crack on the viscoplastic dissipation. $h_s(d^s)$ is the same as the degradation function given in (14).

3.1.3. Evolution of crack fields

By minimization of the total energy functional presented in Equation (6), one gets the governing equations of phase-field evolution:

$$\begin{cases} -\frac{\partial w_e}{\partial d^\alpha} - \frac{\partial w_{vp}}{\partial d^\alpha} - g_c^\alpha \delta_{d^\alpha}\gamma^\alpha = 0 \quad , \quad \dot{d^\alpha} > 0 \quad , \quad \text{in} \quad \Omega \\ -\frac{\partial w_e}{\partial d^\alpha} - \frac{\partial w_{vp}}{\partial d^\alpha} - g_c^\alpha \delta_{d^\alpha}\gamma^\alpha \leq 0 \quad , \quad \dot{d^\alpha} = 0 \quad , \quad \text{in} \quad \Omega \\ \frac{\partial \gamma}{\partial \boldsymbol{\nabla} d^\alpha}.\mathbf{n} = 0 \quad , \quad \text{on} \quad \delta\Omega \end{cases} \tag{22}$$

$\delta_d\gamma$ denotes the variational derivative. Furthermore, the evolution of two crack fields are described by the following equations:

$$\begin{cases} -h_t'(d^t)w_{e+}^0 - g_c^t\left\{\frac{1}{l_d}d^t - l_d div(\boldsymbol{\nabla} d^t)\right\} = 0 \quad , \quad \dot{d}^t > 0 \\ \\ -h_s'(d^s)(w_{e-}^0 + \chi w_{vp}^0) - g_c^s\left\{\frac{1}{l_d}d^s - l_d div(\boldsymbol{\nabla} d^s)\right\} = 0 \quad , \quad \dot{d}^s > 0 \end{cases} \tag{23}$$

where $h_t'(d^t) = -2(1-k)(1-d^t)$ and $h_s'(d^s) = -2(1-k)(1-d^s)$ are the derivatives of two degradation functions with respect to two damage variables.

The evolution of tensile cracks is primarily driven by the elastic strain energy w_{e+}^0, which depends on the tensile (positive) Biot effective stresses $\boldsymbol{\sigma}^{b+}$. Conversely, the progression of shear cracks is influenced by the elastic strain energy w_{e-}^0, associated with compressive (negative) Biot effective stresses $\boldsymbol{\sigma}^{b-}$. However, this outcome from the variational approach does not fully capture the shear cracking mechanism in rocks. It is well-established that shear cracking is typically governed by both the maximum shear stress and compressive mean stress. The classical Mohr-Coulomb criterion, extensively utilized in rock mechanics, encapsulates this physical mechanism. In addressing shear crack evolution, this study proposes a hybrid model. The Mohr-Coulomb criterion is reinterpreted in terms of energy, as detailed in [49], and an alternative driving force w_-^s is defined in the following manner:

$$w_-^s = \frac{1}{2G}\langle \frac{\langle\sigma_1^t\rangle_- - \langle\sigma_3^t\rangle_-}{2cos\varphi} + \frac{\langle\sigma_1^t\rangle_- + \langle\sigma_3^t\rangle_-}{2} tan\varphi - c\rangle_+^2 \tag{24}$$

with the bracket $\langle . \rangle_-$ such as:

$$\begin{cases} \langle a\rangle_- = 0, & a \geq 0 \\ \langle a\rangle_- = a, & a < 0 \end{cases} \tag{25}$$

Here, σ_1^t and σ_3^t are the major and minor Terzaghi effective principal stress. c and φ denote the cohesion and frictional angle of material. By substituting the physically-based driving energy into (23), the criteria for two crack fields are now expressed as:

$$\begin{cases} -h_t'(d^t)w_{e+}^0 - g_c^t\left\{\frac{1}{l_d}d^t - l_d div(\boldsymbol{\nabla} d^t)\right\} = 0 \quad , \quad \dot{d}^t > 0 \\ \\ -h_s'(d^s)(w_-^s + \chi w_{vp}) - g_c^s\left\{\frac{1}{l_d}d^s - l_d div(\boldsymbol{\nabla} d^s)\right\} = 0 \quad , \quad \dot{d}^s > 0 \end{cases} \tag{26}$$

Recognizing crack evolution as an irreversible process, and drawing inspiration from prior research such as [47], the following energy history functionals are introduced:

$$\begin{cases} \mathcal{H}^t(t) = max[w_{e+}^0(\tau)]_{\tau\in[0,t]} \\ \\ \mathcal{H}_-^s(t) = max[w_-^s(\tau)]_{\tau\in[0,t]} \\ \\ \mathcal{H}_{vp}(t) = max[w_{vp}^0(\tau)]_{\tau\in[0,t]} \end{cases} \tag{27}$$

where the time variable τ designates the loading history from the initial state to the current time step t. Using these energy history functionals, the evolution of both tensile and shear cracks is determined by the following relations:

$$\begin{cases} -h_t'(d^t)\mathcal{H}^t - g_c^t\left\{\frac{1}{l_d}d^t - l_d div(\boldsymbol{\nabla} d^t)\right\} = 0 \\ \\ -h_s'(d^s)(\mathcal{H}_-^s + \chi\mathcal{H}_{vp}) - g_c^s\left\{\frac{1}{l_d}d^s - l_d div(\boldsymbol{\nabla} d^s)\right\} = 0 \end{cases} \tag{28}$$

4. Numerical implementation in finite element method

In addressing tensile and shear cracks within thermo-hydromechanical problems, it is necessary to determine five coupled physical fields. Utilizing the finite element method framework, the weak forms of static equilibrium, hydraulic, and heat diffusion equations are articulated as follows:

$$\int_\Omega \delta\boldsymbol{\varepsilon} : \mathbb{C}^b(d^t, d^s) : \boldsymbol{\varepsilon} dV - \int_\Omega \delta\boldsymbol{\varepsilon} : (\delta p)\boldsymbol{I} dV - \int_\Omega \delta\boldsymbol{\varepsilon} : (3\alpha_b K_b(d^t, d^s)T)\boldsymbol{I} dV = \int_{\Omega_f} \boldsymbol{t}.\delta\boldsymbol{u} dS \tag{29}$$

$$\begin{aligned} \int_\Omega \frac{\boldsymbol{\kappa}(d^t, d^s)}{\mu}\nabla p.\nabla(\delta p) dV = &\int_{\Omega_\omega} \frac{\boldsymbol{\kappa}(d^t)}{\mu}\delta p.\nabla p \bar{n} dS - \int_\Omega \frac{1}{M}\frac{\partial p}{\partial t}\delta p dV \\ &- \int_\Omega b\frac{\partial \varepsilon_{kk}}{\partial t}\delta p dV + \int_\Omega 3\alpha_m \frac{\partial \theta}{\partial t}\delta p dV \end{aligned} \tag{30}$$

$$\begin{aligned} \int_\Omega \lambda\nabla T.\nabla(\delta\theta) dV = &\int_{\Omega_q} \lambda\delta T\nabla T.\bar{n} dS - \int_\Omega C_\varepsilon^b \frac{\partial\theta}{\partial t}\delta\theta dV - \int_\Omega (3\alpha_b K_b(d^t, d^s)T_0)\frac{\partial\varepsilon_{kk}}{\partial t}\delta\theta dV \\ &+ \int_\Omega (3\alpha_m T_0)\frac{\partial p}{\partial t}\delta\theta dV + \int_\Omega \frac{\boldsymbol{\kappa}(d^t)}{\mu}\nabla p.(C_p\nabla\theta)\delta\theta dV \end{aligned} \tag{31}$$

$\mathbb{C}^b(d^t, d^s)$ is the drained elastic stiffness tensor of cracked material. This one is affected by the evolution of cracks. Based on the degradation function adopted in (14), one gets:

$$\mathbb{C}_b(d^t, d^s) = \left\{h_t(d^t)\mathbb{P}_\sigma^+ + h_s(d^s)\mathbb{P}_\sigma^-\right\} : \mathbb{C}_b^0 \tag{32}$$

with $\mathbb{C}_b^0$ representing the drained elastic stiffness tensor of the intact material. The permeability tensor of cracked porous media, denoted as $\boldsymbol{\kappa}$, is also influenced by crack growth. For simplicity, yet without losing generality, it is assumed that permeability is predominantly affected by both of tensile cracks and shear cracks. The relationship governing this effect is expressed using the following simple equation [49, 43]:

$$\boldsymbol{\kappa}(d^t) = \boldsymbol{\kappa}_0 \exp(\beta_k max(d^t, d^s)) \tag{33}$$

where the initial permeability tensor of the intact porous medium is denoted as $\boldsymbol{\kappa}_0$, with the parameter β_k controlling its evolution. To simplify the model, it is assumed that the dynamic

viscosity, represented by μ, and the thermal conductivity tensor, λ, remain unaffected by these changes.

On the other hand, based on the governing equations (28), the weak forms for the evolution of tensile and shear crack fields can be written as:

$$\int_\Omega \{(g_c^t/l_d + 2\mathcal{H}_t)d^t\delta d^t + g_c^t\nabla d^t \cdot \nabla(\partial d^t)\}dV = \int_\Omega 2\mathcal{H}_t\partial d^t dV \tag{34}$$

$$\int_\Omega \{(g_c^s/l_d + 2(\mathcal{H}_-^s + \chi\mathcal{H}_{vp}))d^s\delta d^s + g_c^s\nabla d^s \cdot \nabla(\partial d^s)\}dV = \int_\Omega 2(\mathcal{H}_-^s + \chi\mathcal{H}_{vp})\partial d^s dV \tag{35}$$

Employing elementary approximations and appropriate shape functions for each field, combined with an implicit time discretization scheme, leads to the derivation of the following discrete systems of equations tailored for coupled THM problems:

$$\begin{cases} \mathbf{R}_{uu}\Delta\mathbf{U} + \mathbf{C}_{up}\Delta\mathbf{P} + \mathbf{C}_{uT}\Delta\mathbf{T} = \Delta\mathbf{F}_e \\ \mathbf{C}_{pu}\Delta\mathbf{U} + (\Delta\mathbf{t}\mathbf{R}_{pp} + \mathbf{M}_{pp})\Delta\mathbf{P} + \mathbf{C}_{pT}\Delta\mathbf{T} = \Delta\mathbf{t}(-\mathbf{R}_{pp}\mathbf{P} + \Delta\mathbf{F}_\omega) \\ \mathbf{C}_{Tu}\Delta\mathbf{U} + \mathbf{C}_{Tp}\Delta\mathbf{P} + (\Delta\mathbf{t}\mathbf{R}_{TT} + \mathbf{M}_{TT})\Delta\mathbf{T} = \Delta\mathbf{t}(-\mathbf{R}_{TT}\mathbf{T} + \Delta\mathbf{F}_q) \\ \mathbf{K}_{d^t}\mathbf{d}^t = \mathbf{F}_{d^t} \\ \mathbf{K}_{d^s}\mathbf{d}^s = \mathbf{F}_{d^s} \end{cases} \tag{36}$$

The detailed expression of all matrices can be found in Appendix A. Drawing inspiration from earlier research, specifically [36, 54], this study employs an Alternate Minimization (AM) strategy. This approach involves initially determining the THM solutions based on the crack fields obtained in the previous time step. These solutions are then utilized to determine the current crack fields. An iterative loop is employed to update all solutions until they meet the established convergence criteria.

5. Application to HLW disposal analysis [55]

In this section, we present an application example focused on the numerical analysis of thermo-hydromechanical responses and the progression of induced cracks within the framework of the French High-Level Waste disposal concept [55, 56, 57]. The proposed THM model incorporates the double phase field method to simulate this two-dimensional benchmark exercise [57]. This simulation is specifically designed to capture the thermal fracturing of COx claystone. It focuses on the fracturing close to the borehole heater (near field) caused by short-term heating, as well as in the deeper areas distant from the borehole heater (far field), which is induced by long-term heating. It is important to highlight that, drawing upon our prior research [43], the code and material parameters employed in this study have undergone verification. This was achieved through a comparative analysis between pertinent experimental results and an analytical solution.

5.1. Geometry and mesh

The domain under study represents a vertical cross-section at the mid-plane of the HLW disposal cells. It is modeled within the two-dimensional plane, assuming strains perpendicular to this plane are negligible. As depicted in Figure 1, the geometric domain incorporates

a single disposal cell to take advantage of symmetrical properties, given the HLW repository's design with multiple parallel cells. In this study, which focuses on assessing the risk of fractures induced by heating, the disposal cells are positioned 26 meters apart. Accordingly, the width of the study domain is set at 13 meters. To account for the varying effects of different rock layers, a depth of 1000 meters is selected for examining the excavation and heating processes in the HLW disposal cell, which itself has a depth of 560 meters. Specific depths of various geological layers can be found in Table 1.

In this study, the HLW is modeled on the scale of 150-meter-long micro-tunnels, which have an excavated diameter of 0.8 meters. Each micro-tunnel is lined with a 0.025-meter-thick steel casing, resulting in an inner diameter of 0.75 meters. For the sake of simplicity in this benchmark exercise, the gap between the rock and the casing is not considered, implying that no filling material is included in the model. As depicted in Figure 2, the numerical model utilizes a mesh comprising 4508 quadrilateral elements and 4847 nodes, with a finer mesh concentration near the cell.

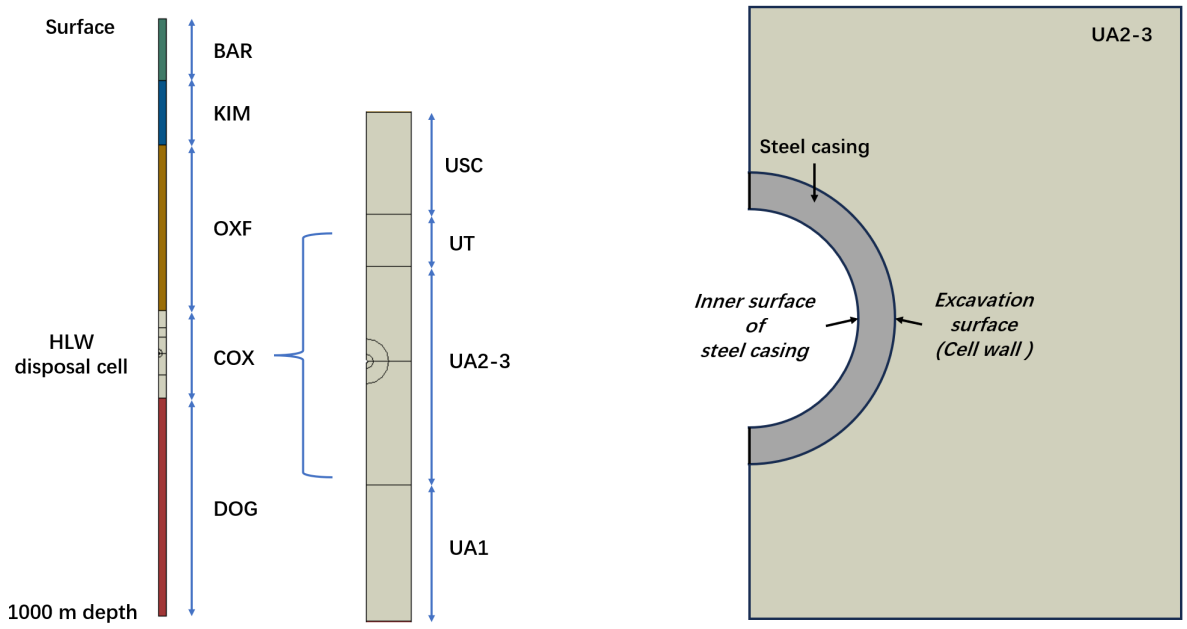

Figure 1: Model domain for the HLW repository test [55]

Table 1: Depth of the different geological layers [55]

	Abbreviation	Depth
Barrois limestone	BAR	0.0 m – 103.4 m
Kimmeridgian	KIM	103.4 m – 211.4 m
Carbonated Oxfordian	OXF	211.4 m – 488.0 m
USC	USC	488.0 m - 517.4 m
UT	UT	517.4 m - 532.6 m
UA2-UA3	UA23	532.6 m - 595.8 m
UA1	UA1	595.8 m - 635.0 m
Dogger	DOG	635.0 m - 1000.0 m

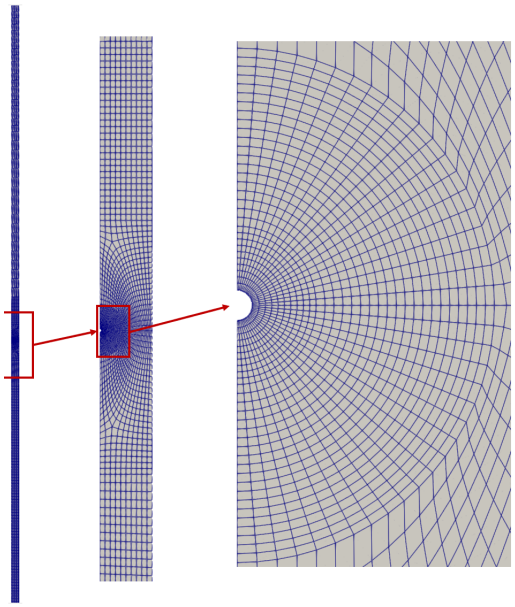

Figure 2: Mesh strategy of simulation

5.2. Initial conditions

The vertical profiles illustrating the initial conditions can be found in Figure 3, providing detailed specifications at the cell level. The temperature distribution across the layers is governed by their respective geothermal gradients, as outlined in Table 2. At a depth of 560 meters, the initial temperature stands at $24.5°C$.

The initial pore pressure p_0 (MPa) displays a gradient relative to depth, set at 0.01 MPa/m. Within the COx layer, an additional overpressure is present. This overpressure increases linearly, reaching a peak of 0.5 MPa at the depth of the cell, corresponding to an overall pressure of 6.1 MPa. It then gradually decreases, eventually reverting to the hydrostatic pressure found within the Dogger layer.

At a given depth, the vertical stress is calculated as the weight of the overburden using the approximation: Vertical stress σ_v (MPa) increases linearly according to the depth with

0.0245 MPa/m. The minimum horizontal stress σ_h is equal to σ_v. And the maximum horizontal stress σ_H (MPa) is equal to the vertical stress in the Kimmeridgian and $1.3 \times \sigma_h$ from top COx.

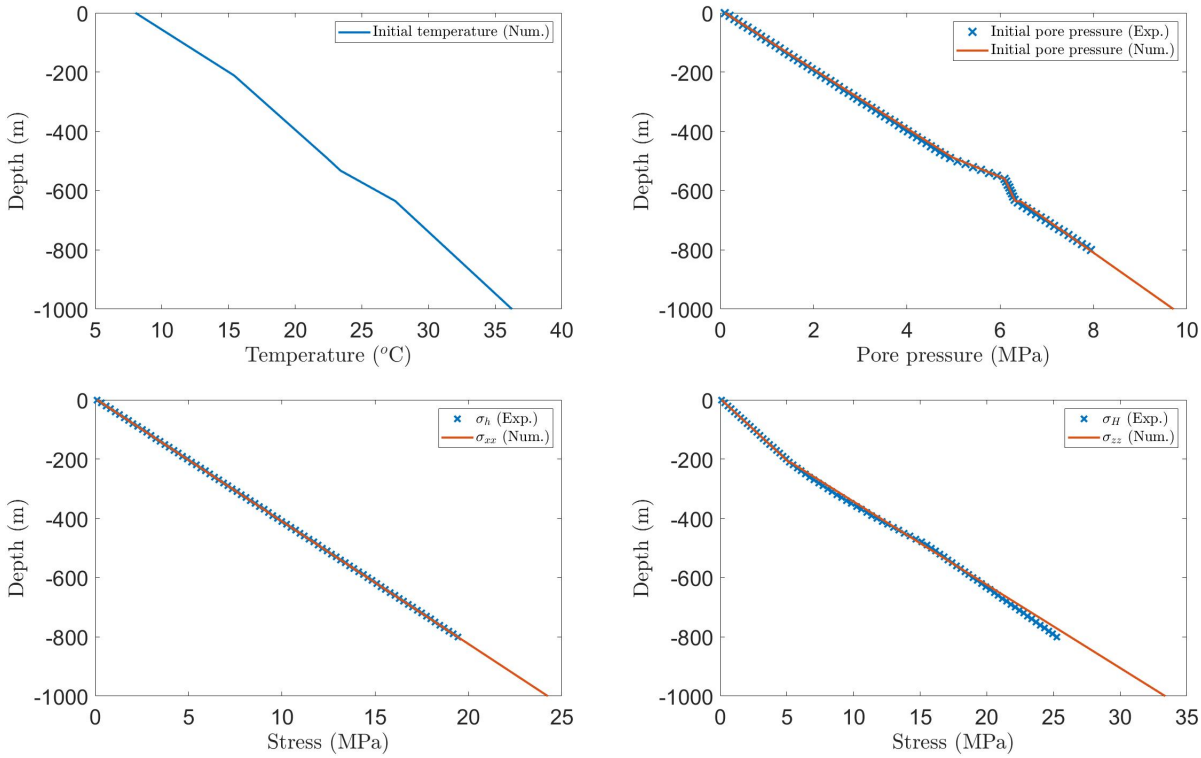

Figure 3: Initial conditions of temperature, pore pressure and stress of the HLW repository simulation, comparing with the measured data

Table 2: Geothermal gradient for each layer $°C/m$

BAR	KIM	OXF	USC	UT	UA23	UA1	DOG
0.035	0.035	0.025	0.024	0.024	0.04	0.04	0.024

5.3. Boundary conditions

In this simulation study, various stages are delineated to represent the drilling and heating processes. These stages are as follows:

- S0: Generation of the initial conditions.
- S1: Drilling of the micro-tunnel.
- S2: Installation of steel casing.
- S3: Emplacement of the HLW packages and commencement of the heating phase.

The boundary conditions, which are independent of these stages, are illustrated in Figure 4-left and elaborated in Table 3. In contrast, the boundary conditions applied to the inner surface of the steel casing and the excavation surface (cell wall) are stage-dependent, as depicted in Figure 4-right.

The initial stage (S0) starts at time t = 0, marking the beginning of micro-tunnel drilling, with a simulation duration of 24 hours. During this phase, the in-situ stress state and pore pressure are set to atmospheric conditions at the cell wall. The installation of the steel casing (S2) is modeled as occurring instantaneously at t = 1 day. This is followed by a period of waiting until t = 2 years, during which a pore pressure of 0.1 MPa is maintained at the cell wall and the inner boundary of the steel casing.

The heating phase (S3) begins at t = 2 years. The thermal history under consideration is based on a HLW package. Once installed in the cell, the thermal load from these packages will gradually diminish over time, a process that is illustrated in Figure 5. In this work, after a cooling period of 85 years, the packages are then installed in the cell.

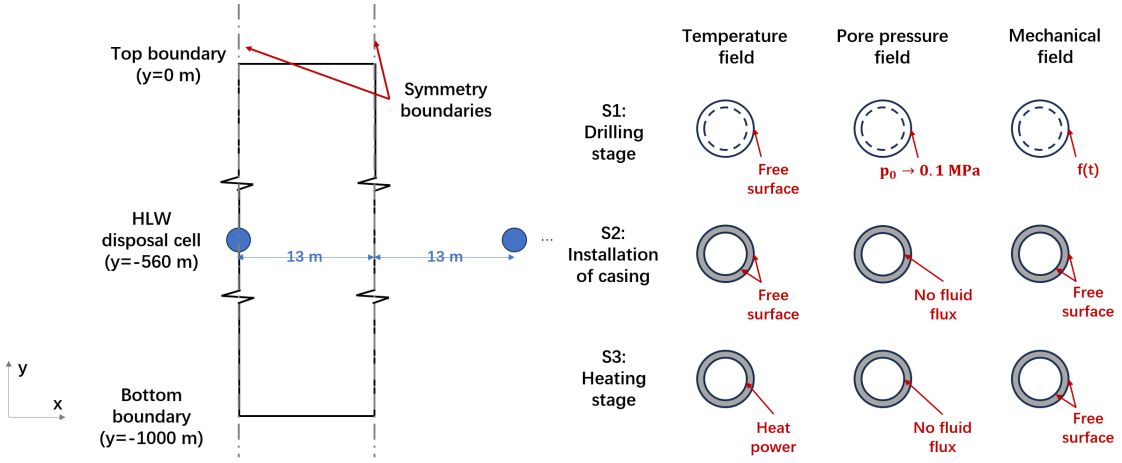

Figure 4: Boundary conditions of the HLW repository test

Table 3: Boundary conditions of HLW repository simulation

Boundary	Thermal	Hydraulic	Mechanical
Symmetry boundaries	No heat flux	No fluid flux	Zero normal displacement
Top boundary	Initial temperature	Initial pore pressure	Free surface
Bottom boundary	Initial temperature	Initial pore pressure	Zero normal displacement

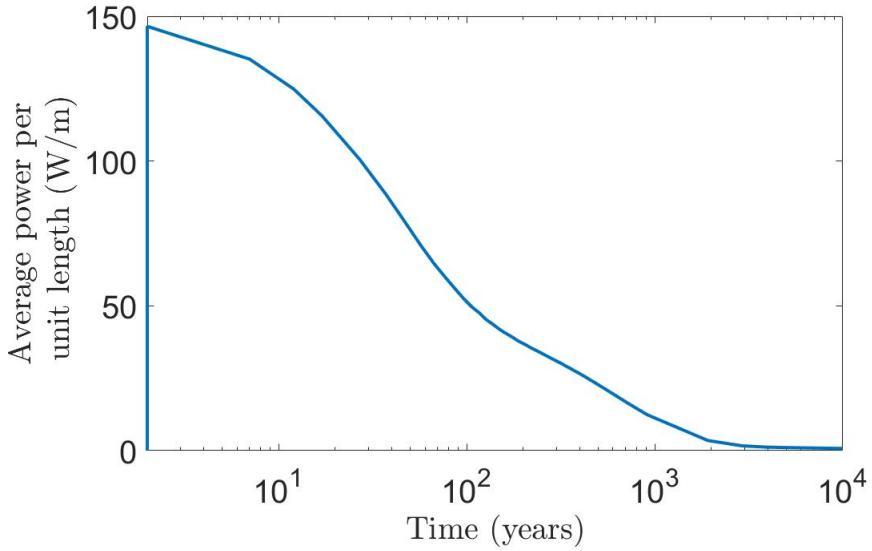

Figure 5: Average power history per unit length of the HLW packages [55]

5.4. Material parameters

The material parameters for the various geological layers are enumerated in Table 4. COx claystone, comprising three sub-layers USC, UT, and UA (including UA1 and UA23) is treated as a transversely isotropic material. The anisotropy ratios for these transversely isotropic materials are provided in Table 5. In contrast, BAR, KIM, and OXF layers are considered isotropic in terms of elastic properties and permeability, but transversely isotropic with respect to thermal conductivity. The DOG layer, on the other hand, is modeled entirely as an isotropic material. Consequently, the shear modulus $G_{\perp\parallel}$ (GPa) for transversely isotropic materials can be effectively approximated using Saint-Venant's formula:

$$\frac{1}{G_{\perp\parallel}} = \frac{1}{E_\perp} + \frac{1}{E_\parallel} + 2\frac{\mu_{\perp\parallel}}{E_\perp} \tag{37}$$

The regular parameters of water are used in this work. For simplicity, the following parameters are considered as constant: bulk modulus of water $K_f = 2.2$ GPa, density of water $\rho_f = 1000$ kg/m^3, heat capacity of water $C_f = 4180$ J/kg/K. The water dynamic viscosity μ_f (Pa·s) is due to temperature T ($^\circ C$), it has:

$$\mu_f(T) = 4.2844 \times 10^{-5} + (0.157(T + 64.993)^2 - 91.296)^{-1} \tag{38}$$

And the volumetric thermal expansion of water α_f ($1/^\circ C$) is also dependent on temperature T ($^\circ C$):

$$\alpha_f(T) = -6T^4 + 1660T^3 - 197796T^2 + 16862446T - 64319951 \tag{39}$$

It should be noted that Equations (38) and (39) delineate the mathematical relationships between μ_f, α_f and T, derived from the trendlines of experimental measurements. As these

equations primarily serve a descriptive purpose based on empirical data and lack direct physical interpretation, there is a discrepancy in the units.

Furthermore, since the phase field method is applied to describe the cracking process in this study, the parameters defined in this numerical method should be chosen carefully as shown in Table 6. The evolution of tensile damage zone is controlled by the material toughness coefficient g_c^t, which cannot be experimentally measured. A widely used equation to define g_c^t is used in this work:

$$g_c^t = \frac{256\sigma_t^2 l_d}{27 E_{eq}} \tag{40}$$

with the average value of uniaxial tensile strength for COx claystone $\sigma_t = 3$ MPa. The equivalent isotropic elastic modulus, E_{eq}, is calculated using the formula $(E_{\parallel} \times E_{\parallel} \times E_{\perp})^{1/3}$. According to Equation (28), the evolution of the shear damage zone is influenced by three parameters: the toughness coefficient of shear damage g_c^s, the friction angle φ, and cohesion c. The rationale for selecting these parameters for COx claystone is detailed in the study cited as [49]. The scale length l_d, which determines the width of localized damage, is set to be twice the size of the mesh elements in the anticipated damage area. Furthermore, the permeability variation coefficient β_k, as defined in Equation (33), was determined from experimental studies [58] and has been successfully applied in previous two-dimensional numerical studies of this rock [49].

Table 6 also presents the viscoplastic parameters employed in this simulation. These parameters were previously used to simulate creep tests for the same rock-like material, COx claystone, as detailed in our earlier work [49]. In that study, the experimental data were successfully reproduced using this set of parameters. The scale length l_d is usually selected to be one to three times the size of the mesh element to effectively capture the damage behavior, as suggested in previous studies [37, 59, 60]. In this study, we have chosen l_d to be twice the size of the element anticipated to be damaged around the micro-tunnel, setting l_d=0.075 m.

Table 4: Reference values of the geological layers for the Base Case

Layer	E_v	v_{hv}	b	ϕ	K_v	ρ_s	λ_v	α_s	$C_{p,s}$
	GPa	-	-	-	$10^{-20}\ m^2$	kg/m^3	$W/m/^\circ C$	$10^{-5\circ}C^{-1}$	$J/kg/^\circ C$
BAR	3.60	0.30	0.80	0.13	10.0	2670	1.10	2.20	848
KIM	3.60	0.30	0.80	0.13	10.0	2670	1.10	2.20	848
OXF	30.00	0.30	0.80	0.13	10000.0	2690	2.30	0.45	745
USC	12.80	0.30	0.80	0.15	1.87	2740	1.79	1.75	772
UT	8.50	0.30	0.80	0.173	1.87	2750	1.47	1.75	735
UA23	4.00	0.30	0.80	0.18	1.33	2770	1.28	1.50	800
UA1	12.5	0.30	0.80	0.164	1.87	2750	1.63	1.75	750
DOG	30.00	0.30	0.80	0.1	100.0	2630	2.30	0.45	788
Casing	200.00	0.30	1.0	0.001	0.001	7850	44.5	1.25	475

Table 5: Reference values of the geological layers for the Base Case

Layer	E_h/E_v	v_{hv}/v_{hH}	K_h/K_v	λ_h/λ_v
BAR	1.00	1.00	1.00	1.40
KIM	1.00	1.00	1.00	1.40
OXF	1.00	1.00	1.00	1.40
USC	1.50	1.50	3.00	1.00
UT	1.50	1.50	3.00	1.50
UA23	1.50	1.50	3.00	1.50
UA1	1.50	1.50	3.00	1.50
DOG	1.00	1.00	1.00	1.00
Casing	1.00	1.00	1.00	1.00

Table 6: Parameter of phase field model and viscoplastic behavior for CRQ simulation

Parameters	Value
Material toughness	g_c^t=1100 N/m; g_c^s=1500 N/m
Friction angle	φ=15°
Cohesion	c=0.1 MPa
Scale length	l_d=0.075 m
Permeability variation	β_k=20
Viscoplastic threshold stress	σ_s=4 MPa
Viscosity coefficient	η=10^7 day^{-1}
Viscoplastic flow rate parameter	n=0.63; m=530

6. Numerical results and analysis

To enhance the clarity and analysis of the numerical results, models that both include and exclude viscoplastic behavior are utilized to simulate the HLW repository benchmark problem. The investigation of THM behavior during the process involves selecting both horizontal and vertical points at various depths near the cell wall. The coordinates of these specific study points are provided in Table 7. Given that a primary objective of this study is to anticipate damage in both the near and far field, the analysis will focus on temperature, pore pressure, displacements, total stresses, and Terzaghi's effective stresses at these particular points.

Table 7: Study points for the numerical results for Step1.3

Point	x-direction (m)	y-direction (m)
P1	0.4	-560.0
P2	1.2	-560.0
P3	6.5	-560.0
P4	13.0	-560.0
P5	0.0	-559.6
P6	0.0	-558.8
P7	0.0	-553.5
P8	0.0	-547.0

6.1. Simulation results without considering viscoplastic behavior

Figure 6, 7 and 8 present simulation results depicting temperature and pore pressure without considering viscoplastic behavior. As illustrated in Figure 6-left, our observations show that the peak temperature, which reaches approximately 88°C, is observed around the 40th year at the proximate points P1 and P5. This peak is followed by a gradual decrease in temperature over time.

There are two noteworthy points to highlight for the temperature results. Firstly, concerning material anisotropy, the evolution and distribution of temperature indicate an anisotropic nature within the high-temperature zone. Specifically, the temperature values in the horizontal direction are notably higher than those in the vertical direction, particularly in distant areas like P4 and P8.

Secondly, regarding the concentrated high-temperature zone as illustrated in Figure 7, it's evident that there exists a pronounced high-temperature zone near the initially heated borehole, as evident in the initial two distribution figures. Remarkably, this heightened temperature gradually extends across the entire domain of this zoomed area, which spans a dimension of 13 meters after 1000 years, as depicted in the final figure.

In terms of pore pressure, Figure 6-right presents the simulation results that do not incorporate viscoplastic behavior. Notably, the overpressure zone exhibits anisotropic behavior, with higher pressures observed in the horizontal direction. This anisotropy is particularly pronounced during the initial phase, before 40 years. The peak pore pressure is recorded at approximately t = 180 years, reaching a maximum of 15.08 MPa. However, as depicted in Figure 8, the pore pressure gradient is significant during the early heating period, such as at 1 year of heating. This gradient diminishes almost completely after 10 years of heating. From 10 years to 180 years, the increase in pore pressure, followed by a subsequent decrease, occurs uniformly across the entire UA2-3 layer. This uniformity is contingent on the boundary condition, specifically the designed distance between two cells.

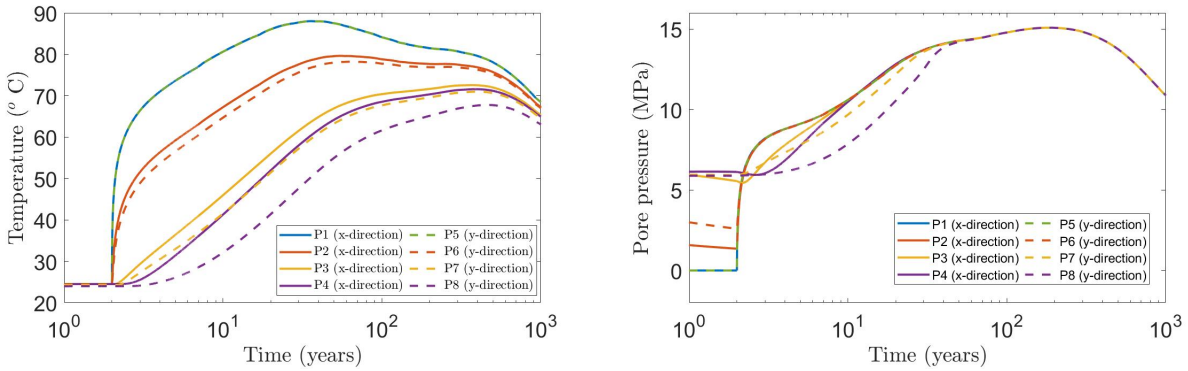

Figure 6: Evolution of temperature and pore pressure versus time without considering viscoplastic behavior

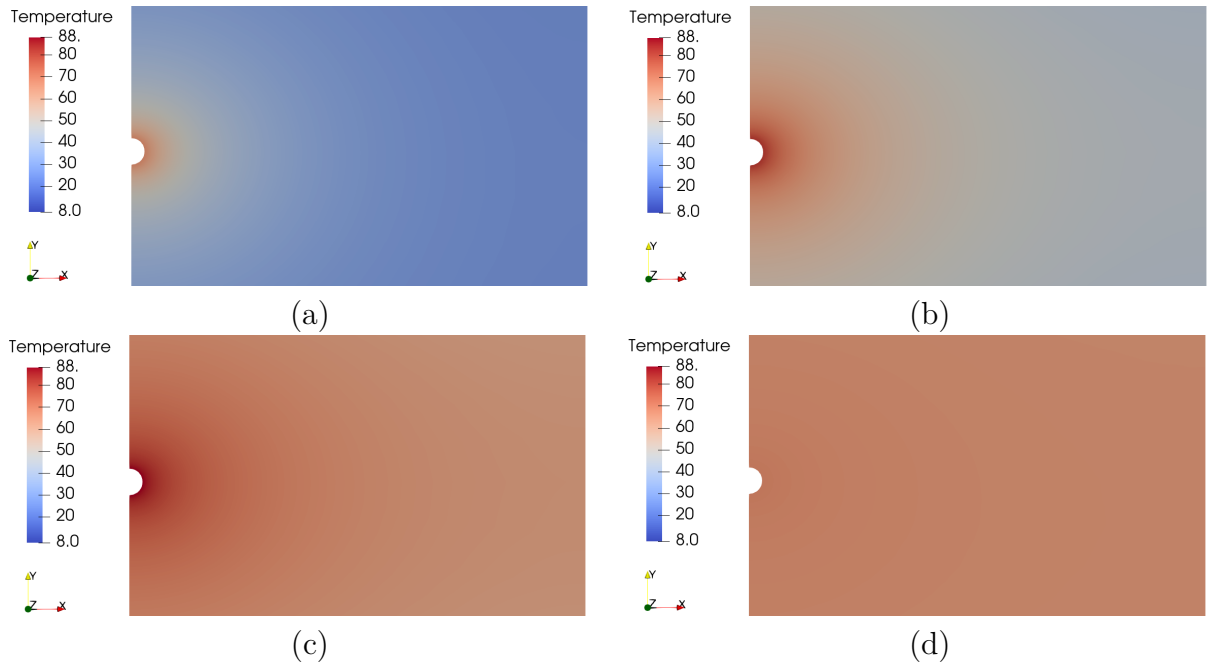

Figure 7: Distribution of temperature at the moment t=1, 10, 40 and 1000 years (without considering viscoplastic behavior)

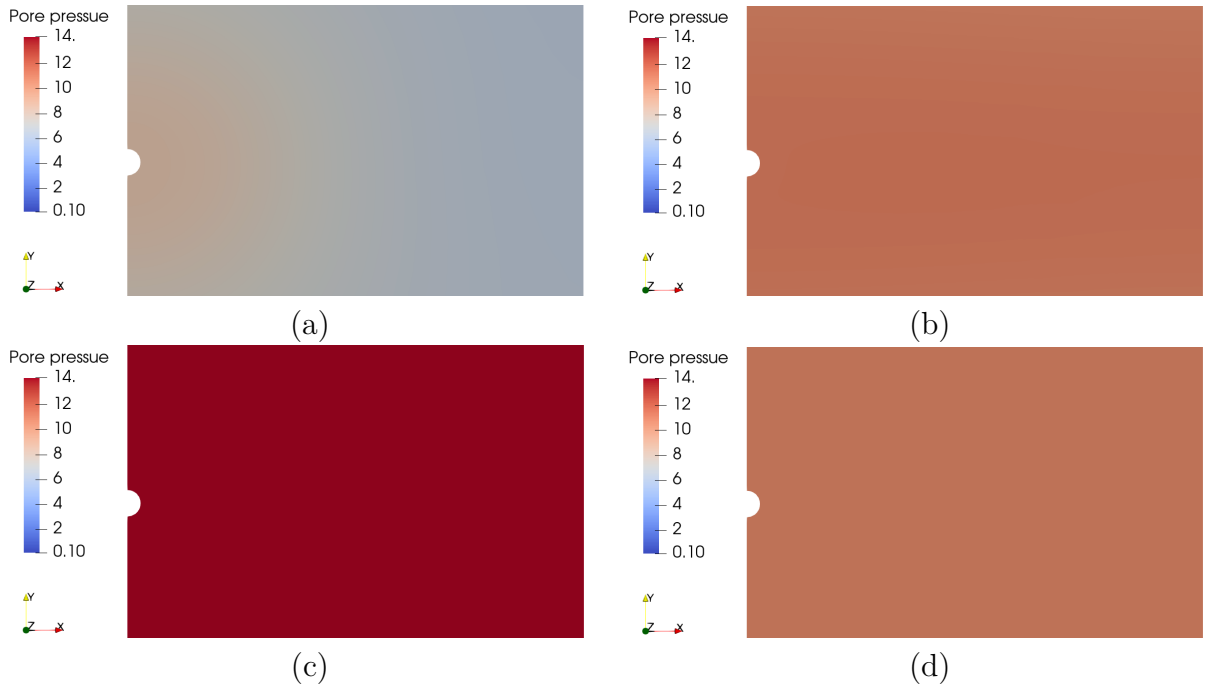

Figure 8: Distribution of pore pressure at the moment t=1, 10, 40 and 1000 years (without considering viscoplastic behavior)

Figure 9 and 10 show the simulation results for distribution of damage. Figure 9 shows the shear damage while Figure 10 shows the tensile damage at four important moments.

In the first moment depicted in figures (a), observed prior to heating, an excavation-induced damaged zone (EDZ) is noticeable. Predominantly, the shear damage zone manifests primarily in the horizontal direction, while no evidence of tensile damage is observed. At this moment, the maximum value of shear damage variable is about 0.26.

Moving on to figures (b), representing the state at 40 years post-heating, coinciding with the period of peak temperature. Here, notable development in shear damage is observed, with the maximum value escalating from 0.26 to 0.45. Additionally, there's initiation of tensile damage induced by the heating, apparent specifically around the heater of cell. The maximum value of tensile damage variable has almost reach to 1.

Figures (c) depict the state at 180 years after heating, a time corresponding to the peak of pore pressure. Compared to the 40-year mark, the shear damage remains unchanged, whereas the tensile damage zone extends deeper, forming two diagonal bands as a result of the heating.

In Figures (d), which illustrate the state 1000 years after heating, the far field is further impacted by this tensile damage zone, exhibiting a variable value of approximately 0.4. It seems that the proximity of the two HLW disposal cells is too close to effectively control the development of fractures.

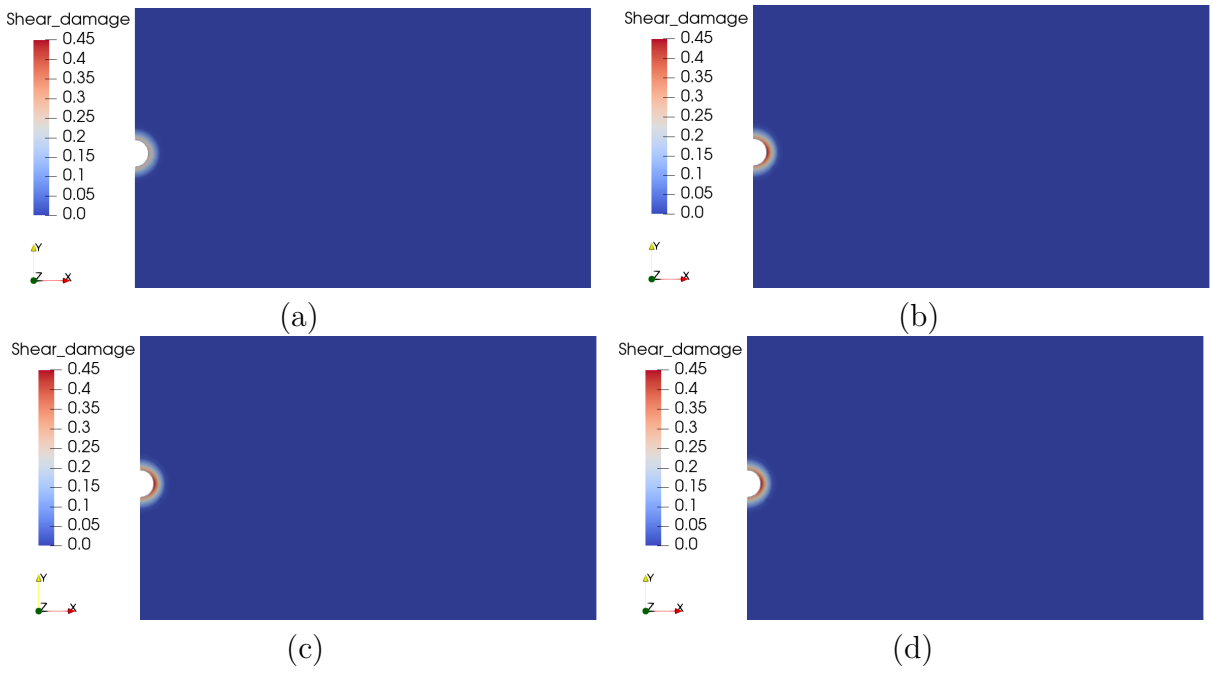

Figure 9: Distribution of shear damage at the moment t=0, 40, 180 and 1000 years

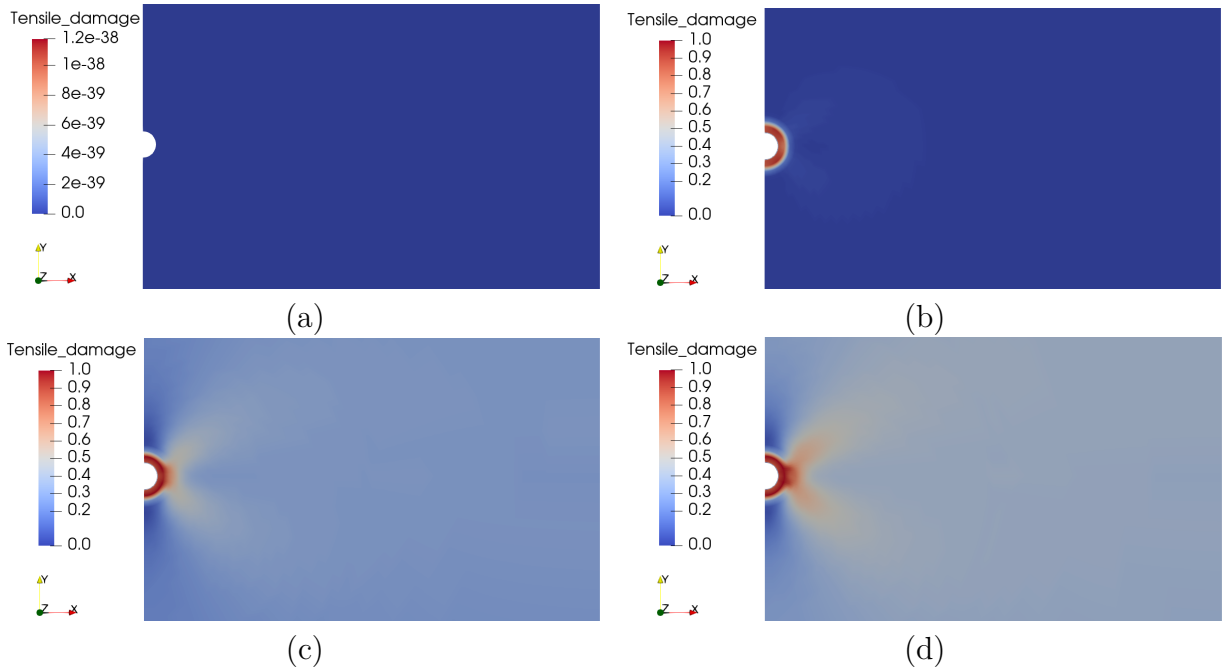

Figure 10: Distribution of tensile damage at the moment t=0, 40, 180 and 1000 years

In further examining the THM behavior influenced by the damage effect, it is observed that the temperature remains constant, as damage does not affect thermal conductivity. However, the evolution of pore pressure is altered when the impact of permeability changes

due to the damage zone is considered. Figure 11 provides a comparative analysis between results obtained from simulations that account for the damage effect and those that do not. Specifically, Figure 11-left presents comparisons at horizontal points, while Figure 11-right focuses on vertical points.

A noticeable trend emerges: the increment in permeability due to damage can reduce pore pressure in long-term behavior, contrasting short-term behavior where such reduction is not observed. This phenomenon can be attributed to the reduced impact of damage, which arises from the impermeable condition at the cell wall caused by the casing, especially in the short term.

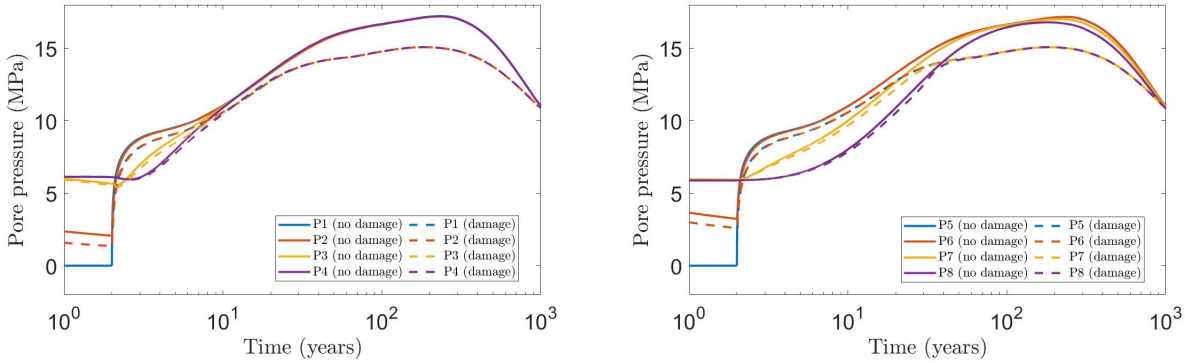

Figure 11: Evolution of pore pressure versus time, comparing between the simulation with and without considering damage effects

Figure 12 illustrates the displacements in horizontal and vertical directions, respectively. Notably, the horizontal displacement of P5-P8 remains fixed due to their designation as boundary conditions, thus not being depicted here. Comparatively, the horizontal displacement is relatively small, largely influenced by the proximity of the two heating cells. Moreover, concerning vertical displacement, it's logical to observe that the displacement of vertical points (P5-P8) surpasses that of horizontal points (P1-P4). Consequently, the maximum vertical displacement at point P8 exceeds 200 mm in this scenario.

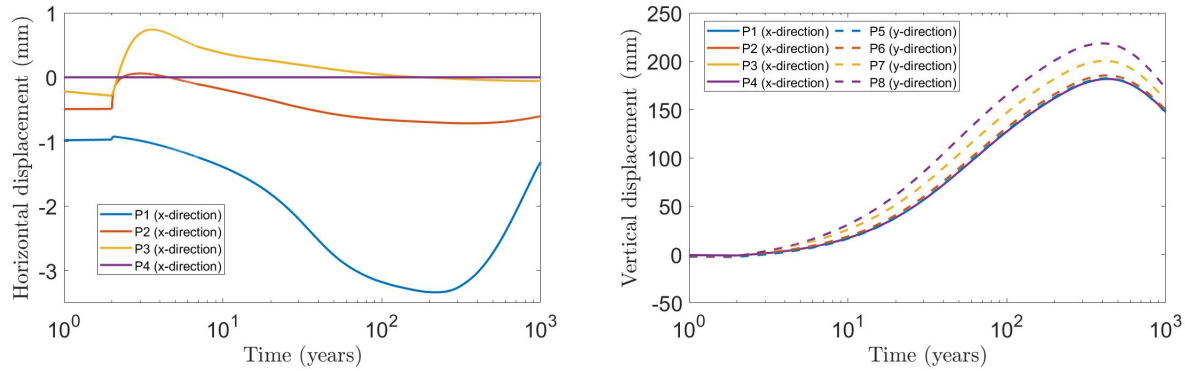

Figure 12: Evolution of horizontal and vertical displacement versus time without considering damage effects

Figures 13 and 14 offer a comparative analysis of the Terzaghi effective stress variation using models that both consider and disregard the damage effect. In Figure 13, which illustrates results from the model without damage consideration, a significant observation is the presence of curves at several points exceeding the tension strength value (σ_t=3 MPa). For example, σ^t_{xx} at point P1 and σ^t_{yy} at points P5 and P6 demonstrate values surpassing this threshold, indicating that heating likely induces failure behavior in these areas. In contrast, after considering the damage effect, Figure 14 shows that, when comparing these curves with those from Figure 13, a clear trend is observed: all curves now fall below the COx claystone's tension strength. This decrease in stress levels can be attributed to the material stiffness degradation caused by localized damage. Therefore, this simulation serves as a validation of our thermo-poro-elastic damage model.

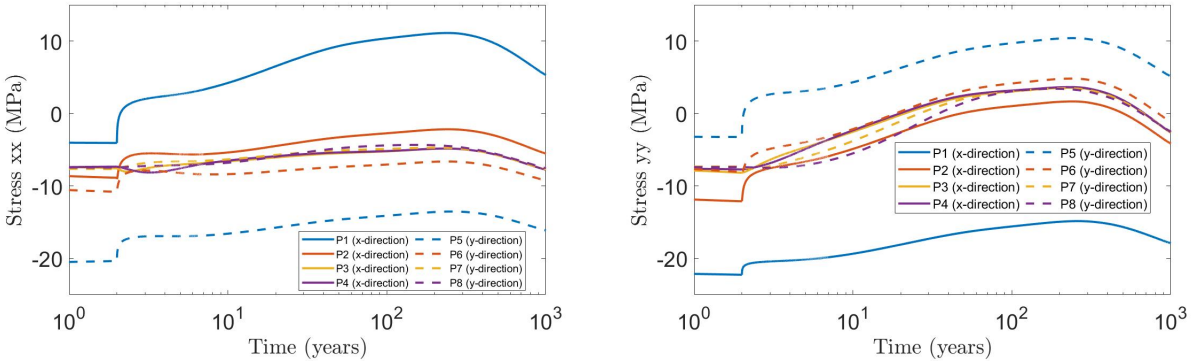

Figure 13: Evolution of Terzaghi effective stress σ^t_{xx} and σ^t_{yy} versus time without considering damage effects

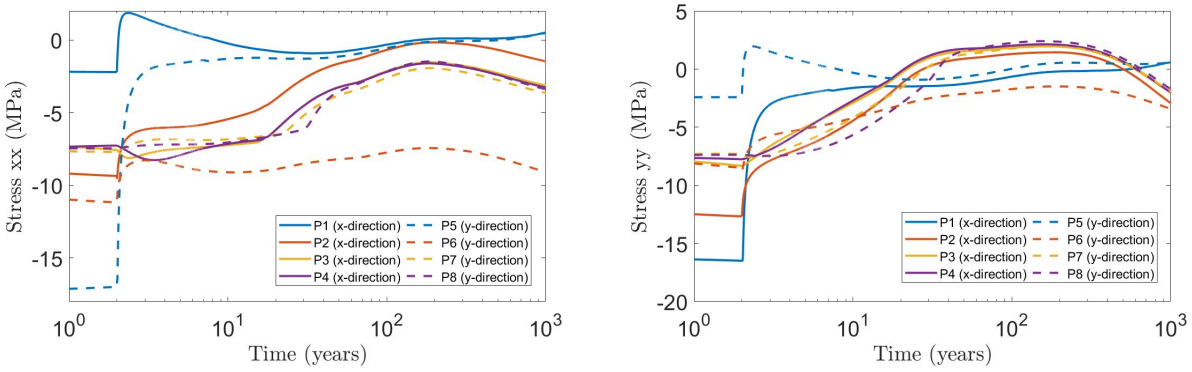

Figure 14: Evolution of Terzaghi effective stress σ^t_{xx} and σ^t_{yy} versus time with considering damage effects

6.2. Simulation results with considering time-dependent behavior

Given that the simulation aims to study rock behavior over a substantial timespan of 1000 years, incorporating time-dependent behavior into the numerical model is crucial. In this section, focusing on the simulation that accounts for damage effects, the inclusion of viscoplastic behavior is comprehensively considered.

Compared to the previous simulation that did not account for viscoplastic behavior, the distribution of tensile damage remains unchanged. We attribute this to the assumption made in Equation (28), where the driving force for tensile damage is not influenced by stored viscoplastic behavior. Figure 15 illustrates the shear damage distribution when simulating with viscoplastic behavior under the assumption that $\chi = 0.1$. Unlike the previous simulation results shown in Figure 9, where the shear damage zone stayed constant during the heating stage, the current simulation reveals an expansion of the shear damage zone in both the near and far fields. In the near field, the shear damage zone extends from the excavation damaged zone horizontally, with the maximum shear damage variable reaching 0.6 in this expanded area. In the far field, the shear damage zone develops toward deeper areas in the form of two diagonal bands, similar to the propagation pattern of tensile damage. Additionally, the far field experiences minor shear damage, with variable values less than 0.1.

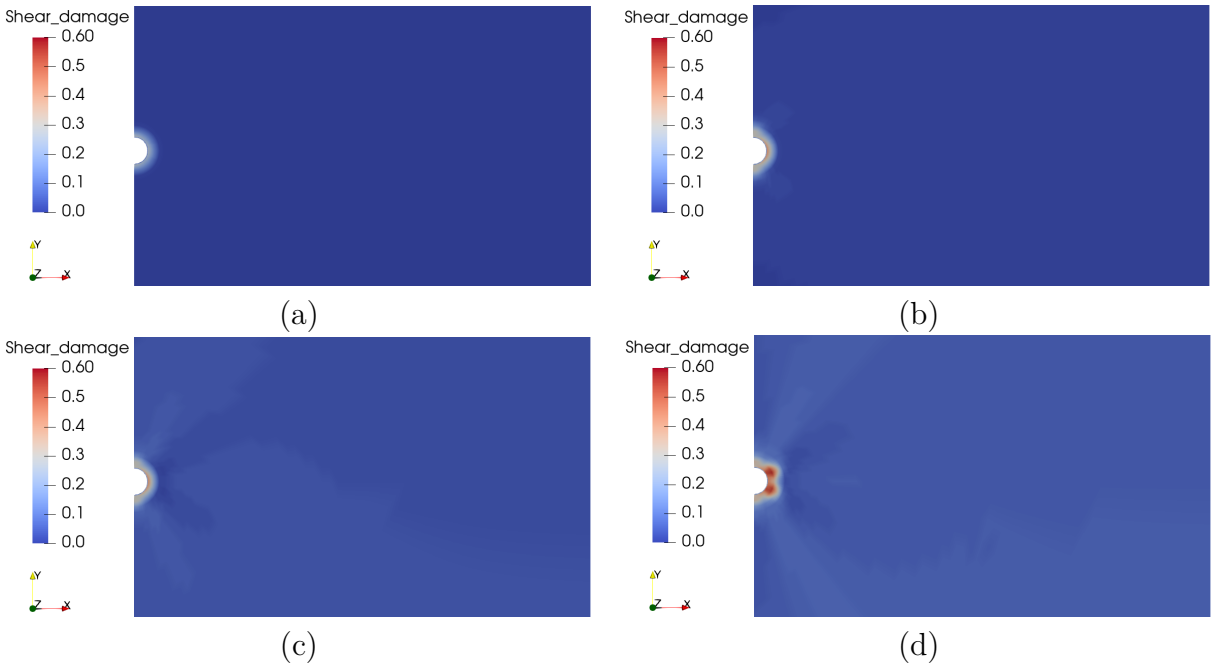

Figure 15: Distribution of shear damage at the moment t=0, 40, 180 and 1000 years considering the time-dependent behavior with χ=0.1

Given the challenge in quantifying the parameter χ, we conducted additional simulations using varied values for this parameter to assess its influence on the contribution of viscoplastic behavior to shear damage development. Figure 16 depicts the distribution of shear damage for χ values of 0.1, 0.2, 0.3, and 0.4. It is evident that increasing the χ value does not alter the shear damage in the near field, where the maximum value remains constant. However, in the far field, the shear damage value intensifies, as do the two diagonal bands. For instance, with $\chi = 0.4$, the shear damage variable can reach nearly 0.2 in the far field. These findings suggest that considering shear damage, influenced by viscoplastic behavior, is a critical factor in designing the spacing between the cells.

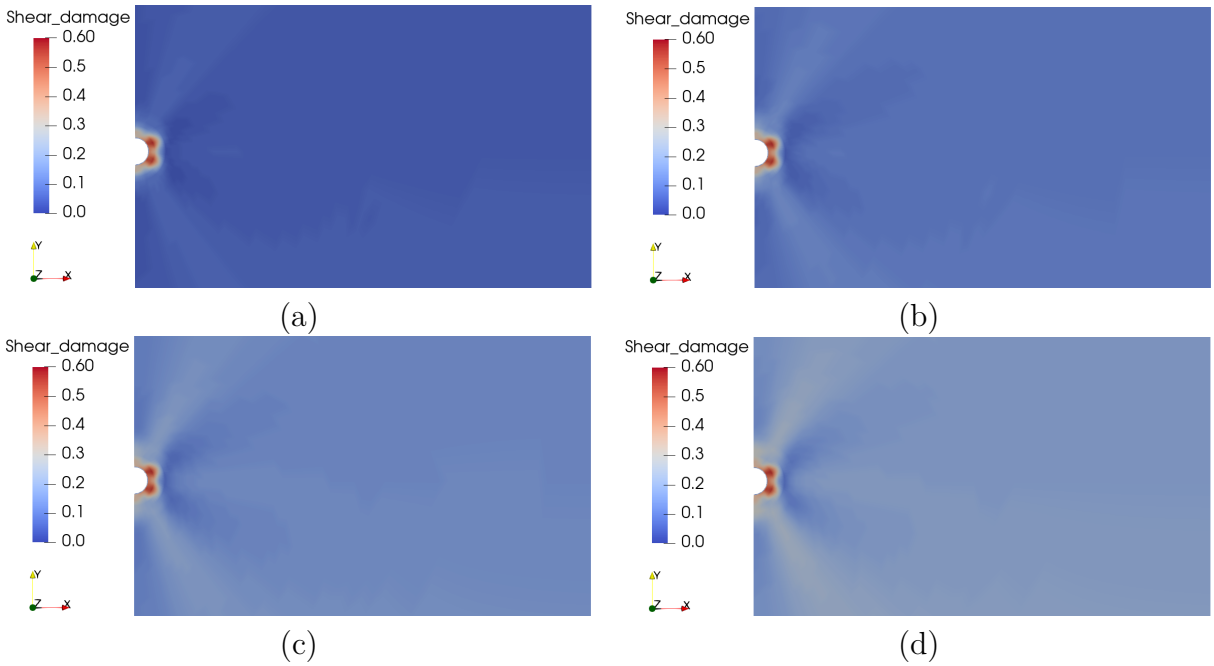

Figure 16: Distribution of shear damage at the moment t=1000 years considering the time-dependent behavior for χ=0.1, 0.2, 0.3, 0.4

Figure 17 compares the pore pressure results from simulations that both incorporate and omit viscoplastic behavior. During the initial 10 years of heating, the pore pressure curves for the studied points in both horizontal and vertical directions are almost identical. However, when viscoplastic effects are considered, the pore pressure reaches its peak at around the 50th year of heating, which is sooner than in the previous simulation. Consequently, the peak value observed is lower, at 13.4 MPa, and this reduced level is also evident at the 1000th year of heating. It is evident that the viscoplastic behavior of the rock reduces pore pressure over the long term. However, this reduction in pore pressure does not diminish the onset of either tensile or shear damage.

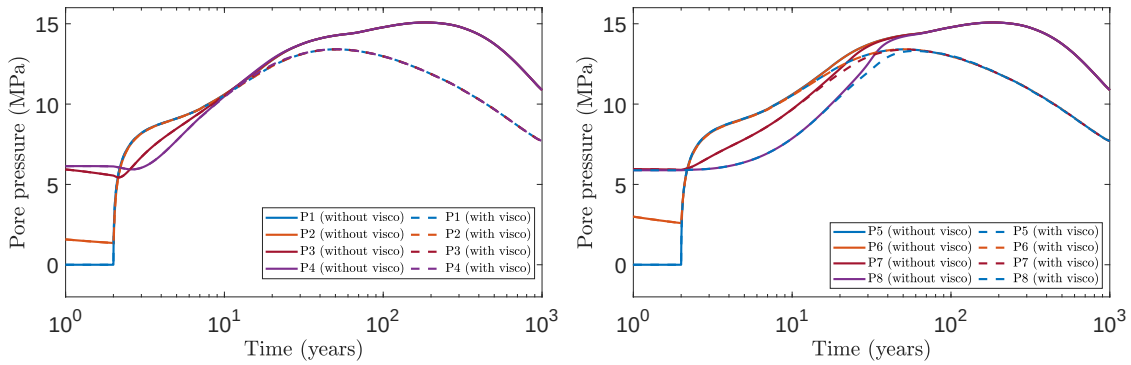

Figure 17: Evolution of pore pressure versus time, comparing between the simulation with and without considering time-dependent behavior

7. Conclusion

The study of thermo-hydromechanical coupling plays a vital role in both the short-term and long-term safety analysis of the geological disposal of radioactive waste. In this context, a THM model has been developed to address both damage and time-dependent behavior in saturated porous media in this work. This model incorporates two independent damage variables, facilitating a comprehensive description of complex cracking processes, including tensile, shear, and mixed-mode cracks. Specifically, the evolution of tensile cracks is driven by tensile elastic strain energy, whereas the development of shear cracks is governed by the generalized Mohr-Coulomb effective shear stress. Additionally, the model accounts for the interaction between shear cracking and viscoplastic flow.

As part of DECOVALEX-2023 Task A, a 2D plane strain benchmark, specifically designed for the scale of a repository, has been proposed. This benchmark necessitated a detailed replication of initial conditions, boundary conditions, and the different layers of rock. During the numerical analysis, two distinct methodologies were employed: a thermo-poro-elastic-damage model both with and without the inclusion of viscoplastic behavior. Each approach was utilized for its respective specialized analysis.

The simulation results reveal a peak in temperature around t = 40 years, followed by a peak in pore pressure at approximately t = 180 years. Notably, at the time when the pore pressure reaches its peak, the Terzaghi effective stress exceeds the tensile strength of COx claystone near the cell wall, indicating potential failure. The proposed thermo-poro-elastic-damage model successfully captures this failure behavior. While the drilling of the micro-tunnel predominantly results in shear damage, the heating process contributes to tensile damage. In the model, the tensile damage variable approaches 1.0 before the peak of pore pressure, signaling the onset of thermal hydraulic fracturing. This cracking process is observed to cause minor damage in the far field. Furthermore, by incorporating time-dependent behavior through a viscoplastic model, the EDZ of shear damage progressively extends toward the far field. This observation leads to the conclusion that a 26-meter distance between two parallel heating cells is insufficient for an effective anti-fracture design.

Acknowledgment:

This work is jointly supported by the French National Agency for radioactive waste management (ANDRA), the DECOVALEX project and the National Natural Science Foundation of China (No. 12202099). DECOVALEX is an international research project comprising participants from industry, government and academia, focusing on development of understanding, models and codes in complex coupled problems in sub-surface geological and engineering applications; DECOVALEX2023 is the current phase of the project. The authors appreciate and thank the DECOVALEX-2023 Funding Organisations ANDRA, BASE, BGE, BGR, CAS, CNSC, COVRA, US DOE, ENRESA, ENSI, JAEA, KAERI, NWMQ, NWS, SURAO, SSM and Taipower for their financial and technical support of the work described in this paper. The statements made in the paper are, however, solely those of the authors and do not necessarily reflect those of the Funding Organisations.

Appendix A: Coefficient matrices for THM-damage coupling problems

$$\begin{cases} \mathbf{R}_{uu} = \int_\Omega ({}^t\mathbf{B}_u)\mathbb{C}^b(d^t, d^s)\mathbf{B}_u dV \\ \mathbf{C}_{up} = \int_\Omega ({}^t\mathbf{B}_u)(-b(d^t))\mathbf{N}_p dV \\ \mathbf{C}_{uT} = \int_\Omega^t \mathbf{B}_u(-3\alpha_b K_b(d^t))\mathbf{N}_p dV \\ \Delta\mathbf{F}_e = \int_{s_t} ({}^t\mathbf{N}_u)\Delta\boldsymbol{t} dS + \int_\Omega ({}^t\mathbf{N}_u)\Delta\mathbf{f}_v dV \end{cases} \tag{41}$$

$$\begin{cases} \mathbf{R}_{pp} = \int_\Omega ({}^t\mathbf{B}_p)(\boldsymbol{\kappa}(d^t, d^s)/\mu)\mathbf{B}_p dV \\ \mathbf{M}_{pp} = \int_\Omega ({}^t\mathbf{N}_p)(\frac{1}{M(d^t)})\mathbf{N}_p dV \\ \mathbf{C}_{pu} = -{}^t\mathbf{C}_{up} \\ \mathbf{C}_{pT} = \int_\Omega ({}^t\mathbf{N}_p)(-3\alpha_m(d^t))\mathbf{N}_p dV \\ \mathbf{F}_\omega = -\int_{s_\omega} ({}^t\mathbf{N}_p)\mathbf{w}_{n+1}.\mathbf{n} dS \end{cases} \tag{42}$$

$$\begin{cases} \mathbf{R}_{TT} = \int_\Omega ({}^t\mathbf{B}_p)(\frac{\lambda}{T_0})\mathbf{B}_p dV \\ \mathbf{C}_{Tu} = -{}^t\mathbf{C}_{uT} \\ \mathbf{M}_{TT} = \int_\Omega ({}^t\mathbf{N}_p)(\frac{C_\sigma^b}{T_0})\mathbf{N}_p dV \\ \mathbf{C}_{Tp} = {}^t\mathbf{C}_{pT} \\ \mathbf{F}_q = -\int_{s_q} ({}^t\mathbf{N}_p)(\mathbf{q}_{n+1}.\mathbf{n}/T_0) dS \end{cases} \tag{43}$$

$$\begin{cases} \mathbf{K}_{d^t} = \int_\Omega \{(g_c^t/l_d + 2\mathcal{H}_t)\mathbf{N}_p^T\mathbf{N}_p + g_c^t l_d \mathbf{B}_p^T\mathbf{B}_p\} dV \\ \mathbf{F}_{d^t} = \int_\Omega 2\mathcal{H}_t\mathbf{N}_p^T dV \\ \mathbf{K}_{d^s} = \int_\Omega \{(g_c^s/l_d + 2(\mathcal{H}_-^s + \chi\mathcal{H}_{vp}))\mathbf{N}_p^T\mathbf{N}_p + g_c^s l_d \mathbf{B}_p^T\mathbf{B}_p\} dV \\ \mathbf{F}_{d^s} = \int_\Omega 2(\mathcal{H}_-^s + \chi\mathcal{H}_{vp})\mathbf{N}_p^T dV \end{cases} \tag{44}$$

$\mathbf{N}_u$ denotes the matrix of shape functions for approximation of displacement components, while $\mathbf{B}_u$ is the matrix of their derivatives to calculate the corresponding strain components. $\mathbf{N}_p$ is the matrix of shape function for approximation of fluid pressure or temperature, and $\mathbf{B}_p$ is the matrix of their derivatives to calculate the corresponding gradient components of fluid pressure or temperature.

References

[1] G. Armand, F. Bumbieler, N. Conil, R. delaVaissiere, J. M. Bosgiraud, M. N. Vu, Main outcomes from in situ thermo-hydro-mechanical experiments programme to demonstrate feasibility of radioactive high-level waste disposal in the callovo-oxfordian claystone., J. of Rock Mechanics and Geotechnical Engineering 9 (2017) 415–427.

[2] Z. B. Liu, S. Y. Xie, J. F. Shao, N. Conil, Effects of deviatoric stress and structural anisotropy on compressive creep behavior of a clayey rock, Applied Clay Science 114 (2015) 491–496.

[3] G. Armand, N. Conil, J. Talandier, D. M. Seyedi, Fundamental aspects of the hydromechanical behaviour of callovo-oxfordian claystone: from experimental studies to model calibration and validation, Computers and Geotechnics 85 (2017) 277–286.

[4] G. Desbois, N. Hohne, J. L. Urai, P. Besuelle, G. Viggiani, Deformation in cemented mudrock (callovo-oxfordian clay) by microcracking, granular flow and phyllosilicate plasticity: insights from triaxial deformation, broad ion beam polishing and scanning electron microscopy, Solid Earth 8 (2) (2017) 291–305.

[5] M. Gasc-Barbier, S. Chanchole, P. Berest, Creep behavior of bure clayey rock, Applied Clay Science 26 (2004) 449–458.
[6] M. Mohajerani, P. Delage, J. Sulem, M. Monfared, A. M. Tang, B. Gatmiri, A laboratory investigation of thermally induced pore pressure in the callovo-oxfordian claystone., Int. J. of Rock Mechanics and Mining Sciences 52 (2012) 112–121.
[7] Z. B. Liu, S. Y. Xie, J. F. Shao, N. Conil, Multi-step triaxial compressive creep behaviour and induced gas permeability change of clay rich rock., Geotechnique 68 (2018) 281–289.
[8] H. Menaceur, P. Delage, A. M. Tang, N. Conil, The thermo-mechanical behaviour of the callovo-oxfordian claystone, International Journal of Rock Mechanics and Mining Sciences 78 (2015) 290–303.
[9] Z. B. Liu, J. F. Shao, Moisture effects on damage and failure of claystone under compression., Geotechnique Letters 6 (2016) 1–5.
[10] Z. B. Liu, J. F. Shao, S. Y. Xie, N. Conil, J. Talandier, Mechanical behavior of claystone in lateral decompression test and thermal effects., Rock Mechanics and Rock Engineering 52 (2019) 321–334.
[11] P. Braun, S. Ghabezloo, P. Delage, J. Sulem, N. Conil, Theoretical analysis of pore pressure diffusion in some basic rock mechanics experiments., Rock Mechanics and Rock Engineering 51 (2018) 1361–1378.
[12] M. N. Vu, G. Armand, C. Plua, Thermal pressurization coefficient of anisotropic elastic porous media., Rock Mech Rock Eng. on line (2019) doi.org/10.1007/s00603–019–02021–1.
[13] P. Braun, P. Delage, S. Ghabezloo, B. Chabot, N. Conil, M. N. Vu, Inducing tensile failure of claystone through thermal pressurization in a novel triaxial device, Rock Mechanics and Rock Engineering 55 (2022) 3881–3899.
[14] N. Conil, M. Vitel, C. Plua, M. N. Vu, D. Seyedi, G. Armand, In situ investigation of the thm behavior of the callovo-oxfordian claystone, Rock Mechanics and Rock Engineering 53 (2020) 2747–2769.
[15] F. Bumbieler, C. Plua, S. Tourchi, M. N. Vu, J. Vaunat, A. Gens, G. Armand, Feasibility of constructing a full scale radioactive high-level waste disposal cell and characterization of its thermo-hydro-mechanical behavior., Int. J. Rock Mech. Min. Sci. (2020) submitted.
[16] C. Plua, M. N. Vu, R. de La Vaissiere, G. Armand, In situ thermal hydrofracturing behavior of the callovo-oxfordian claystone within the context of the deep geological disposal of radioactive waste in france, Rock Mechanics and Rock Engineering online (2023).
[17] D. Seyedi, G. Armand, N. Conil, M. Vitel, M. N. Vu, On the thermo-hydro-mechanical pressurization in callovo-oxfordian claystone under thermal loading., Poromechanics VI 2017 (2017) 754–761.
[18] M. N. Vu, D. Seyedi, G. Armand, Thermo-poro-mechanical coupled processes during thermal pressurization around nuclear waste repository., 6th Coupled Problems in Science and Engineering May 18-20, Venice, Italy (2015).
[19] C.-F. Tsang, O. Stephansson, L. Jing, F. Kautsky, Decovalex project: from 1992 to 2007, Environmental Geology 57 (6) (2009) 1221–1237.
[20] J. T. Birkholzer, A. E. Bond, J. A. Hudson, L. Jing, C.-F. Tsang, H. Shao, O. Kolditz, Decovalex-2015: an international collaboration for advancing the understanding and modeling of coupled thermo-hydro-mechanical-chemical (thmc) processes in geological systems (2018).
[21] J. T. Birkholzer, C.-F. Tsang, A. E. Bond, J. A. Hudson, L. Jing, O. Stephansson, 25 years of decovalex-scientific advances and lessons learned from an international research collaboration in coupled subsurface processes, International Journal of Rock Mechanics and Mining Sciences 122 (2019) 103995.
[22] B. Garitte, T. Nguyen, J. Barnichon, B. Graupner, C. Lee, K. Maekawa, C. Manepally, G. Ofoegbu, B. Dasgupta, R. Fedors, et al., Modelling the mont terri he-d experiment for the thermal–hydraulic–mechanical response of a bedded argillaceous formation to heating, Environmental Earth Sciences 76 (9) (2017) 345.
[23] Z. Yu, J. F. Shao, M. N. Vu, G. Armand, Numerical study of thermo-hydro-mechanical responses of in situ heating test with phase-field model., International Journal of Rock Mechanics and Mining Sciences 138 (2021) 104542.
[24] A. Rodriguez-Dono, Y. Zhou, S. Olivella, A new approach to model geomaterials with heterogeneous properties in thermo-hydro-mechanical coupled problems, Computers and Geotechnics 159 (2023) 105400.

[25] N. Moes, J. Dolbow, T. Belytschko, A finite element method for crack growth without remeshing, Internat. J. Numer. Methods Engrg. 46 (1999) 131–150.
[26] N. Moes, C. Stolz, N. Chevaugeon, P. E. Bernard, A level set based model for damage growth: The thick level set approach, International Journal for Numerical Methods in Engineering 86 (2010) 358–380.
[27] Q. Zeng, J. Yao, J. Shao, An extended finite element solution for hydraulic fracturing with thermo-hydro-elastic–plastic coupling, Computer Methods in Applied Mechanics and Engineering 364 (2020) 112967.
[28] J. Oliver, Modelling strong discontinuities in solid mechanics via strain softening constitutive equations, part 1: fundamentales, Internat. J. Numer. Methods Engrg. 39 (1996) 3575–3600.
[29] Y. Sun, E. Roubin, J. F. Shao, J. B. Colliat, Fe modeling of concrete with strong discontinuities for 3d shear fractures and comparison with experimental results, Engineering Fracture Mechanics 251 (2021) 10775.
[30] Y. Sun, E. Roubin, J. F. Shao, J. B. Colliat, Strong discontinuity fe analysis for heterogeneous materials: The role of crack closure mechanism, Computers and Structures 251 (2021) 106556.
[31] Y. Sun, E. Roubin, J. F. Shao, J. B. Colliat, Meso-scale finite element modeling of the fracture process zone evolution for concrete, Theoretical and Applied Fracture Mechanics 125 (2023) 103869.
[32] S. Silling, Reformulation of elasticity theory for discontinuities and long-range forces, Journal of the Mechanics and Physics of Solids 48 (1) (2000) 175–209.
[33] W. Sun, J. Fish, F. Liu, Y. Lu, A stabilized two-phase pd-fem coupling approach for modeling partially saturated porous media, Acta Geotechnica 18 (1) (2023) 589–607.
[34] T. Ni, X. Fan, J. Zhang, M. Zaccariotto, U. Galvanetto, B. A. Schrefler, A peridynamic-enhanced finite element method for thermo–hydro–mechanical coupled problems in saturated porous media involving cracks, Computer Methods in Applied Mechanics and Engineering 417 (2023) 116376.
[35] G. A. Francfort, J.-J. Marigo, Revisiting brittle fracture as an energy minimization problem, Journal of the Mechanics and Physics of Solids 46 (8) (1998) 1319–1342.
[36] B. Bourdin, G. A. Francfort, J.-J. Marigo, Numerical experiments in revisited brittle fracture, Journal of the Mechanics and Physics of Solids 48 (4) (2000) 797–826.
[37] C. Miehe, M. Hofacker, F. Welschinger, A phase field model for rate-independent crack propagation: Robust algorithmic implementation based on operator splits, Computer Methods in Applied Mechanics and Engineering 199 (45-48) (2010) 2765–2778.
[38] J. Fang, C. Wu, J. Li, Q. Liu, C. Wu, G. Sun, L. Qing, Phase field fracture in elasto-plastic solids: variational formulation for multi-surface plasticity and effects of plastic yield surfaces and hardening, International Journal of Mechanical Sciences (2019).
[39] J. Choo, W. Sun, Coupled phase-field and plasticity modeling of geological materials: From brittle fracture to ductile flow, Computer Methods in Applied Mechanics and Engineering 330 (2018) 1–32.
[40] M. Wang, F. Cormery, W. Q. Shen, J. F. Shao, A novel phase-field model for mixed cracks in elastic–plastic materials incorporating unilateral effect and friction sliding, Comput. Methods Appl. Mech. Engrg. 405 (2023) 115869.
[41] C. Miehe, M. Hofacker, L.-M. Schänzel, F. Aldakheel, Phase field modeling of fracture in multi-physics problems. part ii. coupled brittle-to-ductile failure criteria and crack propagation in thermo-elastic–plastic solids, Computer Methods in Applied Mechanics and Engineering 294 (2015) 486–522.
[42] M. Wang, W. Q. Shen, J. F. Liu, J. F. Shao, Phase-field modeling of cracking process in partially saturated porous media and application to rainfall-induced landslides, Engineering Geology 310 (2022) 106884.
[43] Z. Yu, J. Shao, Y. Sun, M. Wang, M. ngoc Vu, C. Plua, Numerical analysis of hydro-thermal fracturing in saturated rocks by considering material anisotropy and micro-structural heterogeneity, International Journal of Rock Mechanics and Mining Sciences 170 (2023) 105457.
[44] O. Coussy, Poromechanics, John Wiley & Sons, 2004.
[45] A. H.-D. Cheng, Poroelasticity, Vol. 27, Springer, 2016.
[46] Z. Yu, Y. Sun, M. N. Vu, J. F. Shao, Modeling of mixed cracks in rock-like brittle materials under compressive stresses by a double-phase-field method, Rock Mechanics and Rock Engineering online

(2023).
[47] C. Miehe, F. Welschinger, M. Hofacker, Thermodynamically consistent phase-field models of fracture: variational principles and multi-field fe implementations, International Journal for Numerical Methods in Engineering 83 (10) (2010) 1273–1311.
[48] J.-Y. Wu, A unified phase-field theory for the mechanics of damage and quasi-brittle failure, Journal of the Mechanics and Physics of Solids 103 (2017) 72–99.
[49] Z. Yu, J. Shao, G. Duveau, M.-N. Vu, G. Armand, Numerical modeling of deformation and damage around underground excavation by phase-field method with hydromechanical coupling, Computers and Geotechnics 138 (2021) 104369.
[50] P. De Buhan, L. Dormieux, On the validity of the effective stress concept for assessing the strength of saturated porous materials: a homogenization approach, Journal of the Mechanics and Physics of Solids 44 (10) (1996) 1649–1667.
[51] D. Lydzba, J. F. Shao, Stress equivalence principle for saturated porous media, Comptes Rendus Mecanique 330 (4) (2002) 297–303.
[52] S. Y. Xie, J. F. Shao, Experimental investigation and poroplastic modeling of saturated porous geomaterials., International Journal of Plasticity 39 (2012) 27–45.
[53] M. Souley, G. Armand, J.-B. Kazmierczak, Hydro-elasto-viscoplastic modeling of a drift at the meuse/haute-marne underground research laboratoratory (url), Computers and Geotechnics 85 (2017) 306–320.
[54] B. Bourdin, G. A. Francfort, J.-J. Marigo, The variational approach to fracture, Journal of elasticity 91 (1-3) (2008) 5–148.
[55] Eurad wp7 hitec - milestone 49: Selection of benchmark exercises for task 2.3.
[56] C. Plúa, M.-N. Vu, D. M. Seyedi, G. Armand, Effects of inherent spatial variability of rock properties on the thermo-hydro-mechanical responses of a high-level radioactive waste repository, International Journal of Rock Mechanics and Mining Sciences 145 (2021) 104682.
[57] C. Plúa, M. Vu, G. Armand, J. Rutqvist, J. Birkholzer, H. Xu, R. Guo, K. Thatcher, A. Bond, W. Wang, T. Nagel, H. Shao, O. Kolditz, A reliable numerical analysis for large-scale modelling of a high-level radioactive waste repository in the callovo-oxfordian claystone, International Journal of Rock Mechanics and Mining Sciences 140 (2021) 104574.
[58] R. de La Vaissiere, G. Armand, J. Talandier, Gas and water flow in an excavation-induced fracture network around an underground drift: A case study for a radioactive waste repository in clay rock., Journal of Hydrology 521 (2015) 141–156.
[59] M. J. Borden, C. V. Verhoosel, M. A. Scott, T. J. Hughes, C. M. Landis, A phase-field description of dynamic brittle fracture, Computer Methods in Applied Mechanics and Engineering 217 (2012) 77–95.
[60] J. Y. Wu, V. P. Nguyen, C. T. Nguyen, D. Sutula, S. Bordas, S. Sinaie, B. S. P. A, Chapiter one - phase field modeling of fracture, Advances in Applied Mechancis 53 (2020) 1–183.